

NASA Contractor Report 3515

NASA
CR
3515
c.1

TECH LIBRARY KAFB, NM
0062224

A Computer Program for Wing Subsonic Aerodynamic Performance Estimates Including Attainable Thrust and Vortex Lift Effects

LOAN COPY - NOT TO BE
REPRODUCED OR
DISTRIBUTED OUTSIDE
KENT STATE UNIVERSITY

Harry W. Carlson and Kenneth B. Walkley

CONTRACT NAS1-16000
MARCH 1982

NASA



NASA Contractor Report 3515

A Computer Program for Wing Subsonic Aerodynamic Performance Estimates Including Attainable Thrust and Vortex Lift Effects

Harry W. Carlson and Kenneth B. Walkley
Kentron International, Inc.
Hampton, Virginia

Prepared for
Langley Research Center
under Contract NAS1-16000



National Aeronautics
and Space Administration

**Scientific and Technical
Information Branch**

1982

SUMMARY

This report describes numerical methods which have been incorporated into a computer program to provide estimates of the subsonic aerodynamic performance of twisted and cambered wings of arbitrary planform with attainable thrust and vortex lift considerations taken into account. The computational system is based on a linearized theory lifting surface solution which provides a spanwise distribution of theoretical leading-edge thrust in addition to the surface distribution of perturbation velocities. In contrast to the commonly accepted practice of obtaining linearized theory results by simultaneous solution of a large set of equations, the approach used here relies on a solution by iteration. The method also features a superposition of independent solutions for a cambered and twisted wing and a flat wing of the same planform to provide, at little additional expense, results for a large number of angles of attack or lift coefficients. A previously developed method is employed to assess the portion of the theoretical thrust actually attainable and the portion that is felt as a vortex normal force.

INTRODUCTION

The aerodynamic performance of wings at subsonic speeds is critically dependent on the amount of leading-edge thrust that can actually be realized. In reference 1, a study of the factors which place limits on the theoretical leading-edge thrust was made, and an empirical method for estimation of attainable thrust was developed. The applicability of the method was demonstrated by comparisons of theoretical and experimental aerodynamic characteristics for a series of wing-body configurations which employed wings without twist or camber. Suggestions for extension of the method to wings with twist and camber were made.

This report describes numerical methods which have been incorporated into a computer program to permit the analysis of twisted and cambered wings of arbitrary planform with attainable thrust considerations taken into account. The computational system is based on a linearized theory lifting surface solution which provides a spanwise distribution of theoretical leading-edge thrust in addition to the surface distribution of perturbation velocities. In contrast to the commonly accepted practice of obtaining linearized theory results by simultaneous solution of a large set of equations, the approach used here relies on a solution by iteration. The method also features a superposition of independent solutions for a cambered and twisted wing and a flat wing of the same planform to provide, at little additional expense, results for a large number of angles of attack or lift coefficients. A key feature of the superposition technique is the use of leading-edge thrust singularity parameters to identify and separate singular and nonsingular velocity distributions. This separation permits more accurate determination of leading-edge thrust and more accurate integration of pressure distributions for twisted and cambered wings of arbitrary planform. The methods discussed in reference 1 are employed to assess the portion of the theoretical thrust actually attainable and the portion that is manifested as a vortex normal force according to the Polhamus analogy (ref. 2).

SYMBOLS

b	wing span
c	local wing chord
\bar{c}	mean aerodynamic chord
c_{ave}	average wing chord, S/b
c_e	element chord at element midspan
c_A	section axial force coefficient
c_N	section normal force coefficient
$c_{A,C}$	component of c_A due to basic pressure loading of camber surface at 0° angle of attack acting on camber surface
$c_{A,F/C}$	components of c_A due to basic pressure loading of flat wing at 1° angle of attack acting on camber surface
$c_{N,C}$	component of c_N due to basic pressure loading of camber surface at 0° angle of attack acting on camber surface
$c_{N,C,C}$	component of $c_{N,C}$ due to pure camber loading (the contribution with no leading-edge singularity)
$c_{N,C,F}$	component of $c_{N,C}$ due to flat wing loading (the contribution with a leading-edge singularity)
$c_{N,F}$	component of c_N due to basic pressure loading of flat wing at 1° angle of attack acting on camber surface
c_t	theoretical section leading-edge thrust coefficient
$c_{t,a}$	attainable section leading-edge thrust coefficient
c_v	section vortex force coefficient
$c_{t,f}$	theoretical section leading-edge thrust coefficient for a flat wing at 1° angle of attack

C_A	wing axial force coefficient
C_N	wing normal force coefficient
C_D	wing drag coefficient
C_L	wing lift coefficient
C_M	wing pitching-moment coefficient
C_p	pressure coefficient
$C_{p,c}$	pressure coefficient on the cambered wing at 0° angle of attack
$C_{p,f}$	pressure coefficient on the flat wing of 1° angle of attack
$C_{p,c,c}$	component of $C_{p,c}$ due to pure camber loading (the contribution with no leading-edge singularity)
$C_{p,c,f}$	component of $C_{p,c}$ due to flat wing loading (the contribution with a leading-edge singularity)
f	location correction factor for program perturbation velocity (see equation 8)
$F_f(x')$	normal force integration factor for basic pressure loading of flat wing at 1° angle of attack acting on the flat surface (see equation 22). Also used as normal force integration factor for flat wing contribution to the basic cambered wing loading at 0° angle of attack acting on the camber surface; and as axial force integration factor for basic pressure loading of flat wing at 1° angle of attack acting on the camber surface
$F_c(x')$	normal force integration factor for the pure camber contribution to the basic cambered wing loading at 0° angle of attack acting on the camber surface (see equation 25)
$G(x')$	axial force integration factor for basic pressure loading of flat wing at 1° angle of attack acting on the camber surface (see equation 30)

i	index of wing element longitudinal position within the wing program grid system (see figure 1)
j	index of wing element lateral position within the wing program grid system (see figure 1)
k_1, k_2	constants used in definition of camber surface slope
k_c, k_f	constants used in curve fitting of program perturbation velocities and pressure coefficients for integration purposes
M	Mach number
R	Reynolds number
\bar{R}	linearized theory downwash velocity influence function (see equation 4)
S	wing reference area
s	distance along section camber line
Δu	longitudinal perturbation velocity difference across the wing lifting surface as a fraction of the free stream velocity
Δu_c	value of Δu for the cambered wing at 0° angle of attack
Δu_f	value of Δu for the flat wing at 1° angle of attack
u, v, w	perturbation velocities in the x, y , and z directions, respectively
V	free stream velocity
x, y, z	Cartesian coordinates
x'	distance in the x direction measured from the wing leading edge
x'_1, x'_2	x' values at leading and trailing edge of wing element at element semispan
x'_0, x'_1, x'_2	values of x' at which camber surface z ordinates are specified
Δx	longitudinal spacing of grid lines used in establishment of program wing grid system
$\Delta x_C, \Delta x_R, \Delta x_L$	longitudinal distances employed in the influence function \bar{R} [see sketch (d)]

$(\Delta u\sqrt{x'})_0$	limiting value of leading-edge thrust parameter $\Delta u\sqrt{x'}$ at the wing leading edge
$(\Delta u\sqrt{x'})_{0,c}$	limiting value of leading-edge thrust parameter $\Delta u\sqrt{x'}$ at the wing leading edge for the cambered wing at 0° angle of attack
$(\Delta u\sqrt{x'})_{0,f}$	limiting value of leading-edge thrust parameter $\Delta u\sqrt{x'}$ at the wing leading edge for the flat wing at 1° angle of attack
α	angle of attack of wing (in degrees unless otherwise specified)
β	$\sqrt{1 - M^2}$
ϵ	angle between a line tangent to the wing section camber surface and the camber surface reference plane
ϵ_0	value of ϵ at wing leading edge
α_{zt}	angle of attack of wing giving a local theoretical leading-edge thrust of zero for a specified wing spanwise station
Λ	sweep angle of element quarter chord line
Λ_{le}	sweep angle of wing leading edge

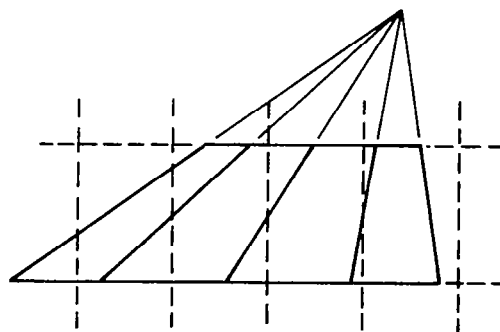
DEVELOPMENT OF COMPUTATIONAL SYSTEM

Development of this method begins with what is believed to be a unique approach to the theoretical analysis of wings at subsonic speeds. Among the features are linearized theory solutions by pure iteration, and the use of leading-edge singularity parameters to identify separate velocity distribution components with and without singularities. The later feature permits more accurate determination of leading-edge thrust distribution for wings with twist and camber and provides for improved pressure distribution integration techniques. The linearized theory solution will be described first, and then attention will be given to the empirical determination of attainable leading-edge thrust and detached vortex flow forces used in the estimation of overall wing performance.

Program Grid System and Wing Definition

The linearized theory solutions are obtained by an iterative solution of influence equations for an array of trapezoidal wing elements representing the actual wing planform as depicted in figure 1. Here only a small number of

elements are shown for the purpose of illustration; in practice several hundred elements would be employed. The elements are superimposed on a rectangular grid so that the inboard and outboard element chords lie along unit values of the spanwise parameter βy and the midspan leading and trailing edges lie on unit values of the chordwise parameter $x/\Delta x$. The scaling of the wing from model or airplane dimensions to program dimensions is chosen to provide the desired number of elements in the spanwise direction. The distance Δx controls the chordwise spacing of the elements; it is selected by specification of an element aspect ratio which is constant for all but the leading-edge and trailing-edge elements. Element corner points at the wing leading and trailing edges are found by interpolation of the scaled program input planform definition. These points determine the leading-edge sweep of the first element and the trailing-edge sweep of the last element in each chordwise row identified by the index $j(\Delta y)$. Sweep angles for elements between the leading- and trailing-edge elements are found from simple geometry for a superimposed arrow wing planform as indicated



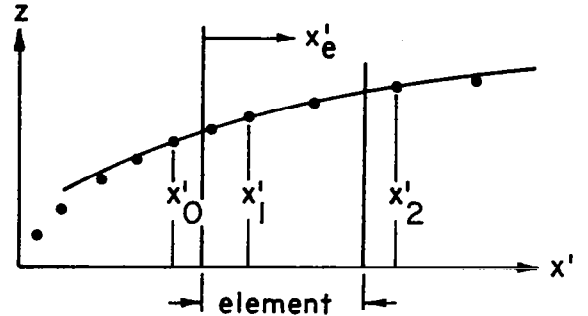
Sketch (a)

in sketch (a). Each element is assigned a number as indicated in figure 1 and a record is kept of the number assigned to the leading- and trailing-edge elements in each chordwise row. The index $i(x/\Delta x)$ is used in determining the order of solution; elements are selected first according to advancing values of the i index then according to advancing values of the j index. The order of solution thus marches front to rear and inboard to outboard.

The wing surface slopes are obtained by a curve fit of interpolated program input camber surface coordinates. The curve fit equation has the form:

$$z = z_0 + k_1(x' - x'_0) + k_2(x' - x'_0)^2 \quad (1)$$

As shown in sketch (b), the interpolated input camber surface ordinates are chosen so as to place one ordinate x'_0 at or ahead of the element leading edge, one ordinate x'_1 within the element and one ordinate x'_2 at or behind the element trailing edge. With the constants k_1 and k_2 chosen to pass the curve through these three points, they can then be used in definition of the element surface slope expressed as:



Sketch (b)

$$\frac{dz}{dx} = k_1 + k_2 x'_e \quad (2)$$

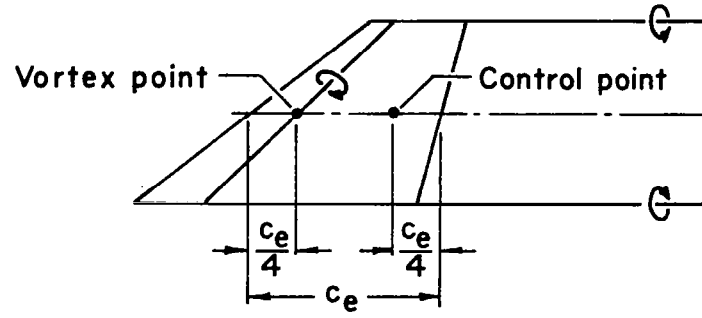
where

x'_e is distance from element leading edge and k_1 and k_2 are redefined to correspond to the new origin

Stored values of $k_{1,e}$ and $k_{2,e}$ allow subsequent recalculation of surface slopes anywhere within the element. The slope at the element three-quarter point is used in satisfying boundary conditions. As will be discussed subsequently, the program repeats the basic linearized theory solution for two wing surfaces. One of these wing surfaces has the slopes described above; the other has a constant slope equal to the tangent of 1 degree angle of attack ($dz/dx = -0.01745$).

Linearized Theory Solution

Each trapezoidal element used to represent the wing is assumed to have an associated horseshoe vortex with a bound leg along the quarter chord line and trailing legs extending to infinity along the extensions of the inboard and outboard chords as shown in sketch (c). At any point in the plane of the wing, the downwash velocity created by the vortex is given by:



Sketch (c)

$$\frac{w}{V} = \frac{-\beta}{4\pi} \bar{R} \Delta u c_e \quad (3)$$

where

Δu is the longitudinal perturbation velocity difference across the wing surface

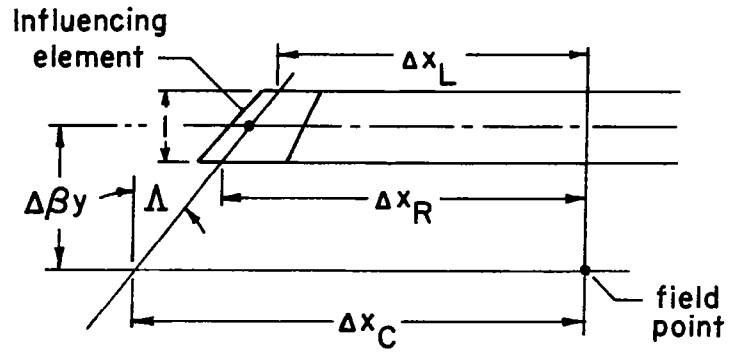
c_e is the element average chord, and

\bar{R} is the influence factor

In terms of the geometry system used here, \bar{R} is given as:

$$\begin{aligned} \bar{R} = & \frac{-1}{\Delta x_C} \left[\frac{(\Delta \beta y + 0.5) + \Delta x_R \tan \Lambda / \beta}{\sqrt{(\Delta x_R)^2 + (\Delta \beta y + 0.5)^2}} \right. \\ & - \frac{(\Delta \beta y - 0.5) + \Delta x_L \tan \Lambda / \beta}{\sqrt{(\Delta x_L)^2 + (\Delta \beta y - 0.5)^2}} \left. \right] \\ & - \frac{1}{(\Delta \beta y - 0.5)} \left[1 - \frac{\Delta x_L}{\sqrt{(\Delta x_L)^2 + (\Delta \beta y - 0.5)^2}} \right] \\ & + \frac{1}{(\Delta \beta y + 0.5)} \left[1 - \frac{\Delta x_R}{\sqrt{(\Delta x_R)^2 + (\Delta \beta y + 0.5)^2}} \right] \end{aligned} \quad (4)$$

The three terms in equation (2) represent, respectively, the bound leg, the left trailing leg, and the right trailing leg. The geometric quantities represented in equation (2) are illustrated in sketch (d). The sign convention is such that the Δx quantities in the sketch are negative. Equation (4) has been obtained by reducing the more general equation (8) of ref. 3 to the planar conditions assumed here.



Sketch (d)

The downwash at any point in the plane of the wing induced by the complete wing may be found by a summation of the contributions of all the individual elements. At the control point of a field point element at which the boundary condition of no flow through the element is to be met, the downwash velocity is given as:

$$\left(\frac{w}{V}\right)^* = \frac{-\beta}{4\pi} \bar{R}^* \Delta u^* c_e^* - \frac{\beta}{4\pi} \sum \bar{R} \Delta u c_e \quad (5)$$

where the starred quantities refer to the field point element and the summation includes all elements but the field point element itself.

The boundary condition is met when

$$\left(\frac{w}{V}\right)^* = \left(\frac{dz}{dx}\right)^*$$

or

$$\Delta u^* = \frac{-4\pi}{\beta} \frac{1}{\bar{R}^* c_e^*} \left(\frac{dz}{dx}\right)^* - \frac{1}{\bar{R}^* c_e^*} \sum \bar{R} \Delta u c_e \quad (6)$$

Before the solution by iteration is begun, perturbation velocities for all elements are set to zero. Then, in the order described in the section "Grid System", each element in turn is considered as a field point element and a perturbation velocity for that element satisfying the boundary condition is found. This new velocity replaces the old one in the velocity table, and the calculation proceeds to the next element. As a means of verifying the solution convergence, the absolute value of the velocity differences between successive iterations is calculated for each element, and an average value of this difference for the whole wing is found. The iteration process is discontinued when for two successive iterations this average difference is less than one-half of one percent (0.005) of the average pressure loading of the flat surface at 1° angle of attack.

As means of reducing computational time, only elements relatively close to the field point are considered in the first iteration. As the iteration process proceeds and the convergence criteria is approached, the region of influence considered is expanded. The influence region is related to the convergence criteria in such a way as to insure that at least for the last two iterations, the whole wing is included. An element is excluded from the summation if:

$$\Delta B_y \text{ is greater than } 4 + 2\sqrt{0.005/CNVGP} \text{ (JB YMAX - 2)}$$

or

$$\Delta x_L \text{ or } \Delta x_R \text{ (whichever is less) is greater than } 2\Delta x + \sqrt{0.005/CNVGP} \text{ (XMAX x SCALE - 2}\Delta x\text{)}$$

where CNVGP is the value of the average difference ratio for the previous iteration, SCALE is the program scale factor, and the other quantities are as defined in the symbol list or in the section "Computer Program."

Correction of Program Results

Because of the element system used to represent the wing, it was known at the outset that there would be errors in the numerical solution in the region of the wing leading edge. It was anticipated that these errors would be systematic in nature and thus predictable so that corrections could be made. Such a strategy was employed in reference 4 for supersonic flow over wings with subsonic leading edges. To study the present numerical solution errors, the programmed solution was modified slightly to permit a solution for a two-dimensional wing. Typical program results for a flat (uncambered) two-dimensional wing at one degree angle of attack are shown in figure 2. Velocity distributions are shown for uniform chord elements at the left of the figure and for a smaller chord first element at the right. The program results are compared with the exact linearized theory solution:

$$\Delta u = 2\alpha \sqrt{\frac{c}{x'} - 1}$$

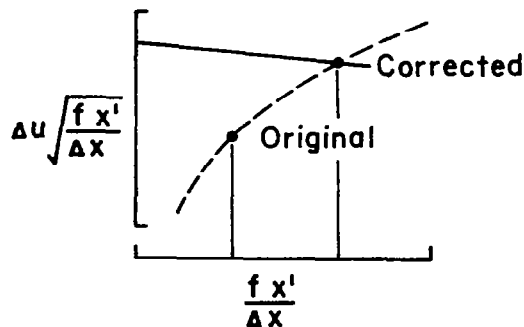
or

$$\Delta u \sqrt{\frac{x'}{c}} = 2\alpha \sqrt{1 - \frac{x'}{c}} \quad (7)$$

with α in radians. The plot of the singularity parameter $\Delta u \sqrt{x'/c}$ allows a more critical comparison of numerical results with the exact linearized theory. The numerical result velocities are assumed to act at the element quarter chord. As shown at the left of the figure, with uniform chord spacing only the first element result is in error. For a smaller first chord as shown at the right, program results for the first two elements (but only the first two elements) behind the leading edge were found to be in error.

When other first element chords were employed, results such as those shown at the upper part of figure 3 were obtained. The well behaved nature of the errors suggested that a correction could easily be made. As in reference 4, the location of the velocity, not its magnitude, is corrected, although for subsonic flow the reasons for this choice are not compelling. As shown in sketch (e), if the location x' is multiplied by a correction factor f , the singularity parameter

now expressed as $\Delta u \sqrt{f x'}$ will follow the dashed curve. Thus it is a simple matter to find a new x' location, defined by the factor f , which will produce agreement with the exact linearized theory. The required factor for each of the program data points is shown at the middle of figure 3. Also shown is a curve fit to the correction factor data defined by:



Sketch (e)

$$f \approx 1 + 0.36 \frac{(1.25 - x'/\Delta x)}{x'/\Delta x} + 0.18 \sin \left(\frac{x'}{\Delta x} \pi \right) \text{ for } x'/\Delta x < 0.5$$

and

(8)

$$f \approx 1 + 0.36 \frac{(1.25 - x'/\Delta x)}{x'/\Delta x} + 0.18 \sin \left(\frac{1.25 - x'/\Delta x}{1.5} \pi \right) \text{ for } x'/\Delta x > 0.5$$

The singularity parameter obtained when the location of the velocity is defined by the factor f is shown at the bottom of figure 3.

It was found that the simple correction derived from the two-dimensional results appeared to be equally valid in three dimensions. Typical program results for constant chord wings (right hand panel only) of various sweep angles at $M = 0$ are shown in figure 4. The singularity parameter is shown as a function of chordwise position for a midspan section. It is seen that there is no erratic behavior of the first two elements. Results for other sweep angles between 0° and 80° and other Mach numbers up to 0.8 were similar.

Convergence of the Iterative Solution

It was found that the iterative solution converged quite rapidly to a reasonable approximation of fully converged results as estimated by extrapolation and as given by vortex lattice matrix inversion methods. However, when stringent convergence criteria are applied, as is required to obtain accurate leading-edge singularity information, a large number of iterations may be necessary. An

example for a 40 degree leading-edge sweep constant chord wing (right hand panel only) is given in figure 5. The first and second iterations give the general character of the solution. More than four iterations are required before sufficiently accurate leading-edge perturbation velocities are provided. The program convergence criteria previously discussed is met after the tenth iteration in this example. For more complex planforms and for severely cambered wings more iterations will be required. For some of the examples shown later up to 50 iterations were required.

Superposition of Cambered and Flat Wing Solutions

In this program, results covering a range of angles of attack are obtained by combining the solution for the input cambered wing (considered to be at 0° angle of attack) with a solution for a flat wing of the same planform at 1° angle of attack. An example of these basic solutions for a 40° swept leading-edge constant chord wing (one panel only) is shown in figure 6. The mean camber surface is defined as an arc of a circle with a radius selected to give a leading edge slope of $dz/dx = 0.0875$ (a 5° angle). Results for the cambered wing are given at the top of the figure, and results for the flat wing are given at the bottom. Note that the cambered wing as well as flat wing displays a leading-edge singularity.

Figure 7 shows results for other angles of attack obtained by combining the cambered and the flat wing solutions by use of the expression:

$$\Delta u = \Delta u_c + \Delta u_f \frac{\sin \alpha}{\sin 1^\circ} \quad (9)$$

The angle of attack of 1.8° was chosen for this illustration because at or near that angle the leading-edge singularity vanishes. The velocity distribution for this case may be considered to be a pure camber loading. For this constant curvature surface, the velocity distribution closely follows a curve defined by:

$$\Delta u = k_c \sqrt{\frac{x'}{c} \left(1 - \frac{x'}{c}\right)}$$

or

$$\Delta u \sqrt{\frac{x'}{c}} = k_c \frac{x'}{c} \sqrt{1 - \frac{x'}{c}} \quad (10)$$

A distribution of this form will be used in the subsequent analysis of leading edge thrust characteristics.

Theoretical Section Thrust Characteristics

Figure 8 illustrates how the angle of attack for a vanishing singularity at a given spanwise station may be found directly. Singularity parameters in the form $\Delta u \sqrt{x'}/\Delta x$ are shown for the first three elements of both the cambered wing at $\alpha = 0^\circ$ and flat wing at $\alpha = 1^\circ$. From previous observations of the nature of cambered and flat wing velocity distributions, it is reasonable to assume a leading-edge singularity parameter of the form:

$$\Delta u \sqrt{x'} = k_f \sqrt{c - x'} + k_c \frac{x'}{c} \sqrt{c - x'} \quad (11)$$

where the first term represents a flat wing contribution and the second term a pure camber contribution. Curve fits of the data for the first two elements using this equation are shown as the dashed lines. The singularity parameter values at the wing leading edge (given by the values of k_f and k_c) will be designated as $(\Delta u \sqrt{x'})_{o,f}$ and $(\Delta u \sqrt{x'})_{o,c}$ for the cambered and flat wing, respectively. It now becomes clear that the angle for a vanishing singularity or, in other terms, the angle for zero leading edge thrust is simply:

$$\alpha_{zt} = \frac{(\Delta u \sqrt{x'})_{o,c}}{(\Delta u \sqrt{x'})_{o,f}} \quad (12)$$

Using relationships developed in reference 5 it may be shown that the section leading-edge thrust coefficient is related to the singularity parameter by:

$$c_t = \frac{\pi}{2} \frac{b}{s} \sqrt{\tan^2 \Lambda_{1e} + \beta^2} [(\Delta u \sqrt{x'})_o]^2 \quad (13)$$

For the flat wing:

$$(\Delta u \sqrt{x'})_0 = (\Delta u \sqrt{x'})_{0,f} \frac{\sin \alpha}{\sin 1^\circ}$$

and

$$c_{t,f} = \left(\frac{\sin \alpha}{\sin 1^\circ} \right)^2 \frac{\pi}{2} \frac{b}{S} \sqrt{\tan^2 \Lambda_{le} + \beta^2} (\Delta u \sqrt{x'})_{0,f}^2 \quad (14)$$

With the definition of α_{zt} and $c_{t,f}$ the section thrust coefficient may be found for any angle of attack by use of the expression:

$$c_t = c_{t,f} \left[\frac{\sin \alpha - \sin \alpha_{zt}}{\sin 1^\circ} \right]^2 \quad (15)$$

The preceding derivations for the evaluation of section thrust characteristics are based on the assumption of constant curvature of the camber surface in the region of the leading edge (a linear variation in the surface slope) for at least the first two elements. For application of the method to severely cambered surfaces, the wing must be composed of a large enough number of elements to provide nearly constant curvature over these first two elements behind the leading edge.

Section Aerodynamic Coefficients

Section aerodynamic coefficients are found by integration of the section pressure distributions, for which the pressure coefficient is assumed to be given by $C_p = 2\Delta u$. Since perturbation velocities are obtained by superposition of cambered and flat wing solutions, the pressure coefficient may be expressed as:

$$C_p = C_{p,c} + C_{p,f} \frac{\sin \alpha}{\sin 1^\circ} \quad (16)$$

or

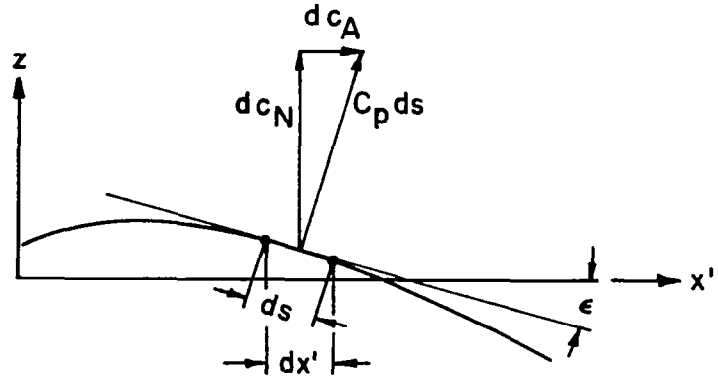
$$C_p = 2 \Delta u_c + 2 \Delta u_f \frac{\sin \alpha}{\sin 1^\circ} \quad (17)$$

As shown in sketch (f) the pressure acting on the airfoil camber surface produces an incremental section normal force given by:

$$dc_N = C_p ds \cos \epsilon = C_p dx'$$

and an incremental section axial force given by:

$$\begin{aligned} dc_A &= C_p ds \sin \epsilon \\ &= -C_p \left(\frac{dz}{dx} \right) dx' \end{aligned}$$



Sketch (f)

The section coefficients may thus be expressed as:

$$c_N = \frac{1}{c_{ave}} \int_0^c C_p dx' \quad (18)$$

$$c_A = \frac{1}{c_{ave}} \int_0^c C_p \left(\frac{dz}{dx} \right) dx' \quad (19)$$

In order to account for leading-edge singularities where appropriate and to avoid them where not appropriate, the integrations are performed by parts.

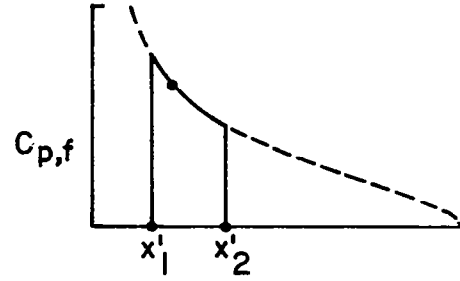
Normal force coefficient. - The total section normal force coefficient (exclusive of thrust or vortex forces) is given by:

$$c_N = c_{N,C} + c_{N,F} \frac{\sin \alpha}{\sin 1^\circ} \quad (20)$$

$c_{N,F}$, the section normal force coefficient generated by the flat wing pressure distribution for 1° angle of attack is obtained by the integration

depicted in sketch (g). Within the limits of a given element (x'_1 to x'_2) the pressure distribution is assumed to have the form:

$$C_p = 2\Delta u = 2k_f \sqrt{\frac{c}{x'} - 1}$$



Sketch (g)

with the constant k_f defined so as to pass the curve through the c_p value at the element quarter chord (or the corrected location for the first two elements). The incremental section normal force for this element is given by the integral:

$$dc_{N,F} = \int_{x'_1}^{x'_2} C_p dx' = 2k_f \int_{x'_1}^{x'_2} \sqrt{\frac{c}{x'} - 1} dx' \quad (21)$$

The integration may be performed through use of the substitutions:

$$\sqrt{\frac{c}{x'} - 1} = \cot \frac{\theta}{2}$$

and

$$dx' = \frac{c}{2} \sin \theta d\theta$$

with

$$\cos \theta = 1 - 2 \frac{x'}{c}$$

The result is:

$$dc_{N,F} = F_f(x') C_{p,f} \quad (22)$$

where

$$F_f(x') = \frac{c}{2} \tan \frac{\theta}{2} [\theta_2 - \theta_1 + \sin \theta_2 - \sin \theta_1]$$

with

$$\theta = \cos^{-1} (1 - 2x'/c)$$

$$\theta_2 = \cos^{-1} (1 - 2x'_2/c)$$

$$\theta_1 = \cos^{-1} (1 - 2x'_1/c)$$

The section normal force coefficient is simply the integral of the incremental coefficients:

$$C_{N,F} = \frac{1}{c_{ave}} \int_0^c dc_{N,F} dx' \quad (23)$$

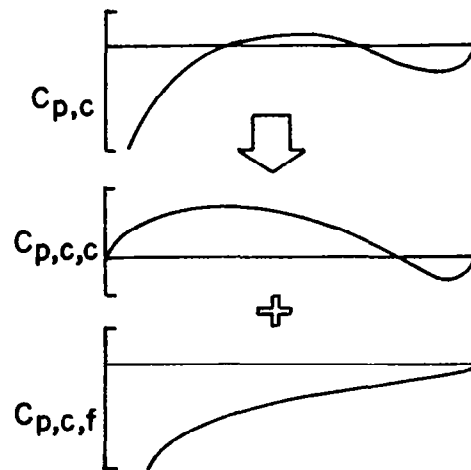
which, as carried out in the program, is merely a summation.

The integration for the cambered wing section normal force is performed in two parts. First, as indicated in sketch (h), the cambered wing pressure distribution is separated into two parts. This is accomplished through use of the angle of attack for a section thrust coefficient of zero:

$$C_{p,c} = C_{p,c,f} + C_{p,c,c}$$

$$C_{p,c,f} = -\alpha_{zt} C_{p,f}$$

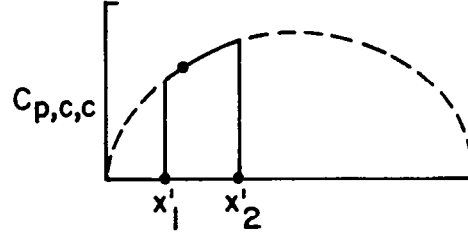
$$C_{p,c,c} = C_{p,c} - C_{p,c,f}$$



Sketch (h)

The integration of the flat plate component, $C_{p,c,f}$ is handled in the same fashion as was the basic flat wing pressure distribution at 1° angle of attack previously discussed to obtain a cambered wing normal force contribution, $C_{N,C,F}$. The integration of the pure camber loading, $C_{p,c,c}$, may be explained through the use of sketch (i). Within the limits of a given element, the pressure distribution is assumed to have the form:

$$C_p = 2\Delta u = 2k_c \sqrt{x'(c - x')}$$



Sketch (i)

with the constant k_c defined so as to pass the curve through the C_p value at the element quarter chord (or the corrected location for the first two elements). The incremental section normal force for the element is given by the integral:

$$dc_{N,C,C} = \int_{x'_1}^{x'_2} C_p dx' = 2k_c \int_{x'_1}^{x'_2} \sqrt{x'(c - x')} dx' \quad (24)$$

On integration:

$$dc_{N,C,C} = F_c(x') C_{p,c,c} \quad (25)$$

where

$$\begin{aligned} F_c(x') = & \frac{c}{2\sqrt{(1 - \frac{x'_1}{c})\frac{x'_1}{c}}} \left[\left(\frac{x'_1}{c} - \frac{1}{2}\right) \sqrt{\left(1 - \frac{x'_2}{c}\right)\frac{x'_2}{c}} \right. \\ & - \left(\frac{x'_1}{c} - \frac{1}{2}\right) \sqrt{\left(1 - \frac{x'_1}{c}\right)\frac{x'_1}{c}} + \frac{1}{4} \sin^{-1}\left(\frac{2x'_2}{c} - 1\right) \\ & \left. - \frac{1}{4} \sin^{-1}\left(\frac{2x'_1}{c} - 1\right) \right] \end{aligned}$$

Then:

$$dc_{N,C} = dc_{N,C,C} + dc_{N,C,F}$$

And:

$$c_{N,C} = \frac{1}{c_{ave}} \int_0^c dc_{N,C} dx' \quad (26)$$

which is obtained as a simple summation.

Axial force coefficient. - The total section axial force coefficient (exclusive of thrust and vortex forces) is given by:

$$c_A = c_{A,C} + c_{A,F/C} \frac{\sin \alpha}{\sin 1^\circ} \quad (27)$$

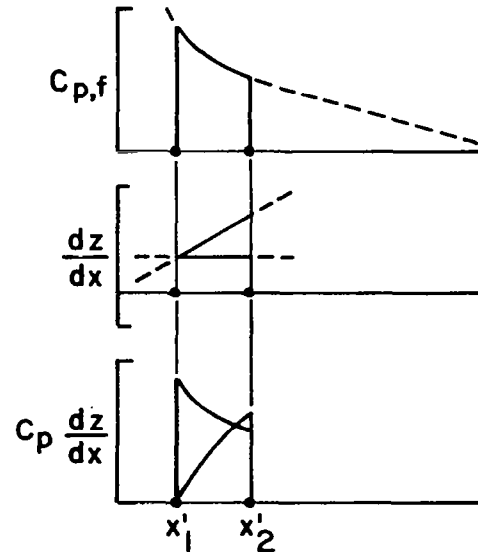
$c_{A,F/C}$, the section axial force coefficient generated by the flat wing pressure distribution for 1° angle of attack acting on the cambered wing surface is obtained by the integration depicted in sketch (j). As before, within a given element the pressure distribution is assumed to have the form:

$$C_p = 2\Delta u = 2k_f \sqrt{\frac{C}{x'} - 1}$$

the camber surface slope within the element is assumed to be expressible as:

$$\frac{dz}{dx} = k_1 + k_2 x'$$

The incremental section interference coefficient for this element is given by the integral:



Sketch (j)

$$\begin{aligned}
dc_{A,F/C} &= - \int_{x_1'}^{x_2'} c_p \left(\frac{dz}{dx} \right) dx' \\
&= -2 k_f k_1 \int_{x_1'}^{x_2'} \sqrt{\frac{c}{x'} - 1} - 2 k_f k_1 \int_{x_1'}^{x_2'} x' \sqrt{\frac{c}{x'} - 1} dx' = dc_{A,F/C,1} + dc_{A,F/C,2}
\end{aligned} \tag{28}$$

With the exception of the factor $-k_1$, the first integral is identical to that for $dc_{N,F}$. Therefore:

$$dc_{A,F/C,1} = -k_f F_f(x') c_{p,f} \tag{29}$$

with $F_f(x')$ as previously defined.

The second term may be integrated to yield:

$$dc_{A,F/C,2} = -k_c G(x') c_{p,f} \tag{30}$$

where

$$G(x') = \frac{c^2}{4} \tan^2 \frac{\theta}{2} [G_1(x_2') - G_1(x_1') + G_2(x_2') - G_2(x_1')]$$

with

$$G_1(x_1') = \left(\frac{x_1'}{c} - \frac{1}{2} \right) \sqrt{\frac{x_1'}{c} - \left(\frac{x_1'}{c} \right)^2}$$

$$G_1(x_2') = \left(\frac{x_2'}{c} - \frac{1}{2} \right) \sqrt{\frac{x_2'}{c} - \left(\frac{x_2'}{c} \right)^2}$$

$$G_2(x_1') = \frac{1}{4} \sin^{-1} \left[2 \left(\frac{x_1'}{c} - \frac{1}{2} \right) \right]$$

$$G_2(x_2') = \frac{1}{4} \sin^{-1} \left[2 \left(\frac{x_2'}{c} - \frac{1}{2} \right) \right]$$

and

$$\cos \theta = 1 - 2 \frac{x}{c}$$

Then:

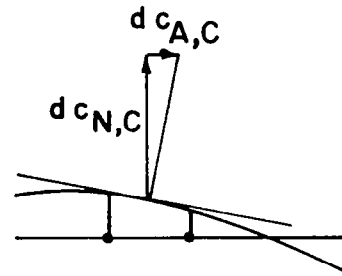
$$dc_{A,F/C} = dc_{A,F/C,1} + dc_{A,F/C,2}$$

And:

$$c_{A,F/C} = \frac{1}{c_{ave}} \int_0^c dc_{A,F/C} dx' \quad (31)$$

is obtained as a summation.

After some unsuccessful initial efforts it was concluded that an analytic basis for pressure integrations to obtain the remaining basic section coefficient, $c_{A,C}$, offered more complications than any benefits would justify. The section axial force due to the cambered wing pressures acting on the camber surfaces is therefore obtained by simpler means. As indicated in sketch (k), $dc_{A,C}$ is calculated from the previously discussed cambered wing section normal force, $dc_{N,C}$, as:



Sketch (k)

$$dc_{A,C} = dc_{N,C} \left(\frac{dz}{dx} \right)$$

with (dz/dx) evaluated at the element midchord.

Then:

$$c_{A,C} = \frac{1}{c_{ave}} \int_0^c dc_{A,C} dx' \quad (32)$$

obtained as a summation.

Section coefficients with thrust and vortex forces. - An overall view of the way the section force coefficient components previously discussed are combined to give total section aerodynamic coefficients (with thrust and vortex forces included) is given in figure 9. The cambered wing at its reference condition (assumed to be 0° angle of attack) produces a normal force $c_{N,C}$. At other

angles the normal force is increased by the flat wing loading increment given by $c_{N,F} \sin \alpha / \sin 1^\circ$. In addition, there may be a small change in normal force due to a component of the attainable thrust acting in the normal force direction $c_t \sin \epsilon_0$. Another, often larger increment, can result from the vortex force c_v that arises when the attainable thrust is less than the full theoretical thrust.

The cambered wing at zero angle of attack produces an axial force $c_{A,C}$. An important interference term contributing to axial force at all other angles of attack is produced by the flat wing loading on the camber surface. That increment is given as $c_{A,F/C} \sin \alpha / \sin 1^\circ$. It is primarily this term which is responsible for the performance benefits of twisted and cambered wings. Finally at angles of attack other than that for section zero thrust, there is an attainable thrust contribution, $c_{t,a} \cos \epsilon_0$.

A sample of the program generated section force coefficients is shown in figure 10. The wing planform used in the program included the fuselage modeled as a wing segment. The most noticeable breaks in the general shape of the distributions are explained by the wing-body juncture at a semi-span fraction of 0.127 and a cambered wing spanwise load distribution that was designed to be constant to the .625 semi-span station and linear from there to the tip. The quantities $c_{t,f}$ and α_{zt} are used as previously described to give theoretical section thrust coefficients as a function of angle of attack.

As has been seen, with the exception of $c_{t,a}$ and c_v , the section force coefficients shown in figure 9 may be obtained by fairly simple operations involving the angle of attack and the basic section parameters illustrated in figure 10. The attainable thrust and the vortex force coefficients, although now predictable at least to a degree, have no simply defined dependence on angle of attack. In employing the method of reference 1 to calculate these coefficients it is necessary to perform separate calculations for each span station at each angle of attack and store the results for subsequent use in the section force coefficient build-up.

Attainable Thrust and Vortex Forces

In reference 1 a study of the factors which place limits on the theoretical thrust was made, and an empirical method for estimating attainable thrust was

developed. The method is based on the use of simple sweep theory to permit a two-dimensional analysis, the use of theoretical airfoil programs to define thrust dependence on local geometric characteristics, and the examination of experimental two-dimensional airfoil data to define limitations imposed by local Mach numbers and Reynolds numbers. This method has been incorporated in the present system but will not be presented here because it is covered in detail in the reference cited.

For wings with sharp leading edges, for which no leading-edge thrust is assumed to develop, Polhamus (ref. 2) established a relationship between the normal force induced by the separated vortex flow and the theoretical leading-edge thrust. According to the Polhamus suction analogy, the suction vector $c_t / \cos \Lambda_{le}$ is assumed to rotate to a position normal to the wing surface, where it affects the normal force rather than the chord force. Because the present method treats a partially developed leading-edge thrust, it seems logical to consider a partial development of the vortex force. The simplest approach is to equate the vortex force with the undeveloped thrust:

$$c_v = \frac{c_t - c_{t,a}}{\cos \Lambda_{le}}$$

This treatment differs from the approach of reference 1, which postulates a gradual rotation of the thrust vector. The present scheme provides a simpler way of handling thrust and vortex forces for wings with twist and camber.

The suction analogy provides no information on the point of application of the vortex force vector. There is an implied assumption that it acts just behind the leading edge. Since the vortex flow field can act at locations which under some conditions may be far removed from the leading edge, accurate estimates of the vortex-induced normal force, and particularly of the axial force, can be made only with some knowledge of the location of the vortex flow field. In the absence of predictive techniques for the vortex location, the vortex force is assumed to act in a direction perpendicular to the wing normal force with no axial force component.

Wing Aerodynamic Coefficients

The program techniques for integration of section forces to obtain overall wing characteristics are very simple. The section coefficients C_N and C_A are assumed to be constant over the span of a given section. Since the section coefficients are non-dimensionalized by the wing average chord, the wing coefficients C_N and C_A for a given angle of attack are determined by a simple summation covering the wing semispan which is then divided by the semispan to produce coefficients based on the reference area. Wing lift and drag coefficients are defined as:

$$C_L = C_N \cos\alpha - C_A \sin\alpha \quad (33)$$

$$C_D = C_N \sin\alpha + C_A \cos\alpha \quad (34)$$

Computer Program

A computer program entitled "Attainable Aerodynamic Performances of Wings at Subsonic Speeds" which combines the linearized-theory wing solution with the methods for estimation of attainable thrust and vortex lift effects may be obtained for a nominal fee from:

Computer Software Management and
Information Center (COSMIC)
112 Barrow Hall
University of Georgia
Athens, GA 30602
(404) 542-3265

Request the program by the designation LAR 12987. This program is written in FORTRAN IV for use on the Control Data 6600 and Cyber series of computers.

Data are input in namelist form under the code INPT1. The wing planform information is specified by a series of leading- and trailing-edge breakpoints. Up to 21 pairs of coordinates may be used to describe the leading edge and up to 21 pairs to describe the trailing edge. The planform input data in program terminology are:

NLEY	number of leading-edge breakpoints (limit of 20)
TBLEY	table of leading-edge y-values in increasing order of y from wing root to wing tip
TBLEX	table of leading-edge x-values corresponding to the TBLEY table
NTEY	number of trailing-edge breakpoints (limit of 20)
TBTEY	table of trailing-edge y-values in increasing order of y from wing root to wing tip
TBTEx	table of trailing-edge x-values corresponding to the TBTEY table
XMAX	largest x-ordinate occurring anywhere on the planform
SREF	wing reference area for use in aerodynamic force and moment coefficients
CBAR	wing reference chord for use in aerodynamic moment coefficients
XMC	x-location of moment reference center
ELAR	desired element aspect ratio (an element aspect ratio approximately one-half the full wing aspect ratio is recommended)

The size of the wing in program dimensions is controlled by the entry:

JBymax integer designating the number of elements in the spanwise direction (see fig. 1) (limit of 41)

The necessary scaling is done within the program by use of a scale factor $2(JBymax)/(\text{SPAN} \times \beta)$. The number of complete wing elements N corresponding to a given JByMAX may be approximated as

$$N = 4 \times JBymax^2 \times \frac{ELAR}{\text{wing aspect ratio}}$$

The program has been written to accommodate 2000 right hand panel elements. Except in very special cases the JByMAX integer will be much less than the limit of 41. The normal range is 10 to 25. Computational costs tend to increase as the square of the number of elements and the fourth power of JByMAX.

The wing section mean camber surface must be specified by exactly 26 chordwise ordinates at up to 21 span stations. When fewer than 26 camber coordinates are used to define the sections, the ordinate tables must be filled with enough zeros to complete the list of 26. The necessary section information is:

NYC	number of spanwise stations at which chordwise sections are used to define the mean camber surface (limit of 21)
TBYC	table of y-values for the chordwise camber surface sections, increasing order of y from root to tip
NPCTC	number of chordwise stations used in mean camber surface definition (limit of 26)
TBPCTC	table of chordwise stations, in percent of chord, at which mean camber surface ordinates are defined; in increasing order from leading to trailing edge
TZORDC	table of mean camber surface z-ordinates corresponding to the TBPCTC table; the full 26 values for the root chord (including zeros for values in excess of NPCTC) are given first, followed by similar information for all spanwise stations in increasing order of y
NYT	number of spanwise stations at which chordwise sections are used to define the thickness distribution (limit of 21)
TBYT	table of y-values for the chordwise thickness distribution sections, increasing order of y from root to tip

The TZORDC table may be multiplied by a scale factor TZSCALE if desired. This may be useful if the original tabulated ordinates are nondimensionalized with respect to a single measurement (the wing root chord, for example) or if it is necessary to evaluate the effect of change in camber surface severity.

The following wing section information is required for the calculation of attainable leading-edge thrust.

NYR	number of spanwise stations at which airfoil section information is supplied (limit of 21)
-----	--

TBYR	table of y values for airfoil section information, increasing order of y from root to tip
TBTOC	table of airfoil maximum thickness as a fraction of the chord
TBETA	table of the section location of maximum thickness as a fraction of the chord
TBROC	table of the leading-edge radius as a fraction of the chord

The flight or test conditions are specified as:

XM	free-stream Mach number
RN	free-stream Reynolds number (based on \bar{c}) in millions, $R/10^6$
NALPHA	number of angles of attack to be calculated (limit of 20)
TALPHA	table of angles of attack to be calculated

The program provides for a maximum of 50 iterations. If this number is reached without the convergence criteria being met, the results for the 50th iteration will be printed with a warning of the failure to meet criteria. If desired, the maximum number of iterations may be increased or decreased by an entry ITRMAX.

The commonly accepted practice of performing subsonic calculations for a Mach number of 0.0 is not appropriate for this program. Program results for $M = 0.0$ will be provided, but the attainable thrust will be zero. Realistic estimates of attainable thrust can be made only if both the Mach number and the Reynolds number correspond to actual conditions.

The printed program results include:

- (1) An iteration by iteration history of the convergence parameters.
- (2) A listing of theoretical pressure distributions for the camber surface at 0° angle of attack and for the flat surface at 1° angle of attack. For each of the program spanwise stations (controlled by JBYMAX), interpolated or extrapolated pressure coefficients are given for a set of chordwise stations. Interpolation or extrapolation is based on the assumption of curves of the form

$$C_p = k_c \sqrt{\frac{x'}{c}(1-\frac{x'}{c})} \text{ for the cambered wing and } C_p = k_f \sqrt{\frac{c}{x'}-1} \text{ for the flat wing.}$$

(3) A listing of the spanwise distribution of section normal, axial, and pitching moment coefficients for the cambered wing at 0° angle of attack and the flat wing at 1° angle of attack. The interference axial force coefficient due to the flat surface loading acting on the camber surface and the theoretical thrust parameters $C_{t,f}$ and α_{zt} are also printed.

(4) A listing of wing overall theoretical aerodynamic coefficients C_N , C_A , C_M , C_L , and C_D with no thrust and with full theoretical thrust as a function of angle of attack.

(5) A listing of wing overall estimated aerodynamic coefficients C_N , C_A , C_M , C_L , and C_D with attainable thrust and vortex lift effects as a function of angle of attack. Attainable thrust and vortex force contributions are listed separately.

Additional printed output data may be selected by use of the following print options:

- IPRCPD = 1 theoretical pressure distributions for each of the selected angles of attack.
- IPRSLDT = 1 theoretical span load distributions of C_N , C_A , C_M , C_L , and C_D with no thrust and with full theoretical thrust for each of the selected angles of attack.
- IPRSLDA = 1 estimated span load distributions of C_N , C_A , C_M , C_L , and C_D with attainable thrust and vortex force effects for each of the selected angles of attack.

COMPARISONS WITH EXPERIMENTAL DATA

The applicability of the present method to practical problems can be assessed by means of a series of comparisons of predictions with experimental measurements presented in figures 11 to 16. The data presented is for axial and normal force as a function of angle of attack and drag as a function of lift. Consideration of axial and normal force is believed to offer a more fundamental study of the

nature of the forces acting on the wing than does an immediate consideration of lift and drag. The program provides pitching moment data, but pitching moment correlations are not shown here. A careful estimate of pitching moment would require consideration of the contributions of more configuration components than can be handled in the present single lifting surface representation. In addition, the pitching moment is sensitive to the location of the vortex force, and although the present method provides an approximation of the magnitude of this force, it provides no information on its location. In these figures the curves labeled "present method" have been obtained by use of the computer program described in this report. The vortex force contribution to the present method result is shown as a shaded band because of some uncertainties as to the proper method of handling it.

In the early stages of the development of this method the vortex force was assumed to act at the wing leading edge where it produced a significant axial force in addition to the normal force. This, however, was found to produce results inconsistent with the experimental data. Because, in general, the vortex will act well aft of the leading edge over a region of the wing where it is likely to produce little or no axial force, only the normal force induced by the vortex is now considered. There is a need for simple empirical methods which can provide estimates of the location of the vortex action line.

No estimated skin friction and form drag contributions to the coefficients have been made. For the comparisons with experimental data shown in this report, the axial force at zero angle of attack has been set equal to the experimental value. However, where comparisons have been made for twisted and cambered wings and for flat wings of the same planform, C_A at $\alpha = 0^\circ$ was determined from experimental data for the flat wing only, so that in those cases predictions of camber induced drag are those given by the present method.

Sketches included in the figures show the actual model planforms and the program planforms which attempt to model the fuselage as well as the wing. Mean camber lines for the fuselage as well as the wing are used in defining the program lifting surface shape. For each of the examples treated, at least two computer runs were made to insure that the mathematical representation was adequate. Consecutive runs with the total number of elements differing by a factor

of two were made and the results accepted only if the differences in all the pertinent coefficients (those illustrated in figure 9) were judged to be small. In all cases but one, which will be discussed in detail, this test could be met with a reasonable number of elements and reasonable computational costs.

A comparison of program results with experimental data from reference 6 for both a flat and a twisted and cambered delta wing of aspect ratio 2 in combination with a simple body of revolution is shown in figure 11. The wing incorporated a 5 percent thick NACA 0005-63 section. The twisted and cambered wing was designed for a trapezoidal spanwise load distribution at a Mach number of 1.53 and a design lift coefficient of 0.25. The data presented are for a Mach number of 0.61 and a Reynolds number of 3.0×10^6 . In examining first the flat wing data and in particular the axial force, it is seen that nearly full thrust is developed over only a small angle of attack range, and that only a small portion of the theoretical thrust is developed at the largest angles shown. The present method gives a reasonable estimate of the thrust actually produced. Because of the failure to produce thrust, a separated leading-edge vortex would be expected which in turn would produce a non linear increase in normal force. The normal force data indicate that such a vortex force actually is present, and is predicted by the present method. The method, however, does not consider the vortex location and thus can lead to prediction of too large an increment at large angles where much of the vortex structure may actually be aft of the wing trailing edge. The present method is seen to provide a good estimate of the lift-drag performance of this wing-body combination. The no thrust and full thrust limits provide a broad range of aerodynamic performance possibilities, and thus a reasonably accurate determination of attainable thrust is a critical part of the estimation process.

For the twisted and cambered wing [fig. 11(b)] the axial force curve is quite different. It is no longer symmetrical, and has more negative values of the coefficient at moderate and large angles. The theory indicates that even without thrust, negative values of axial force could be achieved. As might be expected, for equal values of theoretical thrust, the fraction attainable for the cambered wing is not far different than that for the flat wing. The experimental increment in axial force at zero angle of attack is seen to be larger than the increment predicted by the program. As for the flat wing, there

seems to be a vortex contribution to the normal force. Again there is a good correlation of the experimental drag and the program predictions, except near zero lift.

Similar data for a wing body combination (ref. 7) with an aspect ratio 4 delta wing are shown in figures 12(a) and 12(b). This wing also employed a NACA 0005-63 section. The twisted and cambered wing of the pair was designed for a spanwise trapezoidal load distribution at a Mach number of 1.15 and a lift coefficient of 0.35. The data presented are for a Mach number of 0.25 and a Reynolds number of 8.0×10^6 . As can be seen in both parts of this figure, this wing at a lower Mach number and at a larger Reynolds number than for the first example, achieves a considerably greater thrust force which is well predicted up to an angle of attack of about 12 degrees. The predicted vortex normal force fails to materialize, perhaps due to vortex bursting. For both the flat and the twisted and cambered wing, the lift-drag polar prediction is good up to lift coefficients of about 0.6. Note that for the flat wing C_D follows the full thrust curve very closely up to a lift coefficient of about 0.25 and that the twisted and cambered wing displays nearly full thrust to a C_L of about 0.35. Beyond these points the breakaway is pronounced.

Data for a supersonic cruise fighter design from reference 8 are shown in figure 13. The blended wing-body model incorporated an under the fuselage engine inlet. The wing camber surface was determined from mean ordinates of cross sections with the duct intake area removed. The test conditions are $M = 0.60$ and $R = 2.8 \times 10^6$. Except for a prediction of too large a normal force at zero angle of attack and a small underestimation of the attainable thrust at moderate angles of attack, the correlation is not far different than those shown previously. The lift-drag polar prediction is good through most of the lift coefficient range shown.

A rather complex high performance supersonic transport configuration from reference 9 is treated in the example shown in figure 14. This configuration incorporated a twisted and cambered wing, a cambered fuselage, engine nacelles, and horizontal and vertical tails. The nacelles and the horizontal and vertical tails can not be represented at all in the single lifting surface provided for in the program. In the determination of normal force, the horizontal tail was

treated separately, and its normal force was added without interference to that of the wing (about a 5% increase in wing normal force at a given angle of attack). No other account of these additional components was made. Apparently only a small amount of the theoretical leading-edge thrust was achieved and that only for small angles of attack. The reason for this is not known. Because the present method overestimates the thrust it necessarily underestimates the vortex lift increments. These errors tend to compensate one another in the evaluation of drag and thus the method still gives a reasonable prediction of the lift-drag polar. The prediction tends to fall below the experimental data because the benefits of a given increment in thrust are greater than the benefits of a corresponding increase in normal force.

Up to this point, the correlation examples have treated vehicles designed for supersonic cruise. For this class of vehicle with relatively thin wing sections, the degree of attainment of leading-edge thrust may vary greatly with changes in geometric properties of the wing and with changes in operational conditions. Thus the present capability for prediction of attainable thrust and vortex effects for twisted and cambered as well as flat wings is a valuable asset.

The subsonic transport wing-body example from reference 10 treated in figure 15 presented a most difficult challenge for the present numerical method. The problem lay in the nature of the wing mean camber surface. First, the camber surface slope was quite large (about 0.3) at the wing leading edge, and second, the variation of this slope with distance behind the leading edge could be considered to be linear for only 3 or 4 percent of the chord. It will be recalled that one assumption used in the derivation of the method for evaluation of leading-edge thrust called for a linear variation of camber surface slope over at least the first two elements. Even with the 1788 total wing elements used in the computer run for which data are presented, this condition could not quite be met. Differences in computed results for different numbers of elements (and different chordwise spacing) indicated, however, that the solution was nearly converged.

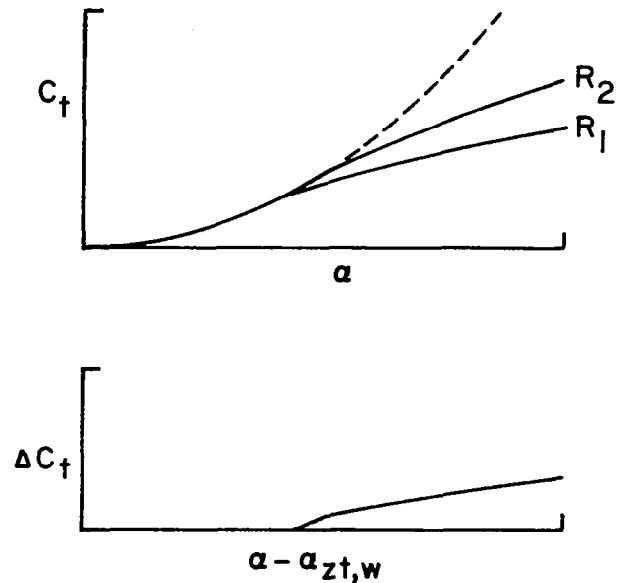
In figure 15 note the steep slope of the no thrust axial force line. This, in addition to the theoretical thrust contribution, is one of the key elements provided by the linearized theory solution. If the program results as well as

the experimental data are to be believed, the wing-body achieves essentially 100 percent of the theoretical thrust up to the largest angle for which data are given. The attainable thrust prediction shows a reduction in the attainable thrust percentage to about 84% at 6° angle of attack. This difference in axial force, although it may appear to be small, is almost entirely responsible for the difference between predicted and measured drag in the lift-drag polar.

The final example provides something close to an ultimate test for this computational system. In figure 16 program results are compared with measured data from reference 10 for a full-scale airplane tested in the NASA Langley Full Scale Wind Tunnel. The airplane is an advanced technology twin engine general aviation aircraft. For the test data shown here the horizontal tail was removed but all other components including the "stopped" propellers were in place. The program wing planform is complex and the mean camber surface which accounts for the over-the-wing nacelles has a rather severe shape. As shown in figure 16, the correlation between the predicted and the experimental data is poor. The source of the disagreement is directly traceable to the slope of the normal force coefficient. The predicted leading-edge thrust is too large because the section loadings and thus the singularity strengths are too large. An analysis of this same configuration presented in reference 11 experienced the same difficulty in prediction of normal force. An account of boundary-layer effects on the effective airfoil profile made in that report produced a somewhat better agreement, but at large angles the normal force was still overestimated. The problem may be due to flow separation caused by unpredictable nacelle, fuselage, and wing interactions.

It is seen that vehicles designed for subsonic cruise present a more difficult problem than vehicles designed for supersonic cruise. Their thicker wing sections are more difficult to handle properly in the numerical solution without a large number of elements and increased computational costs. Furthermore, the thicker wings tend to produce leading-edge thrust close to the full theoretical values so that estimation of attainable thrust is not as critical a factor. Even so, some of the techniques presented here may prove to be valuable additions to other computational methods that perhaps are more suited to the geometric characteristics of subsonic cruise aircraft.

For a given configuration, the attainable thrust increases with increasing Reynolds number. Thus extrapolation of wind-tunnel data to full scale flight conditions requires consideration of this effect. The computing program described herein provides a means of performing the extrapolation. Because only increments in thrust are required, modeling of a wing alone with no twist or camber is sufficient. As shown in sketch (1) the increment in thrust coefficient is found as the difference between computer runs for the wind tunnel and the flight Reynolds number. The increment is applied to the wind-tunnel axial force data as a function of the absolute value of $\alpha - \alpha_{zt,w}$ where $\alpha_{zt,w}$ is a measure of an effective or average angle of attack for zero thrust for the wing as a whole. For a wing without twist or camber this angle is zero. For a twisted and cambered wing, as shown in sketch (m), the angle $\alpha_{zt,w}$ may be found by fitting a curve of the form:



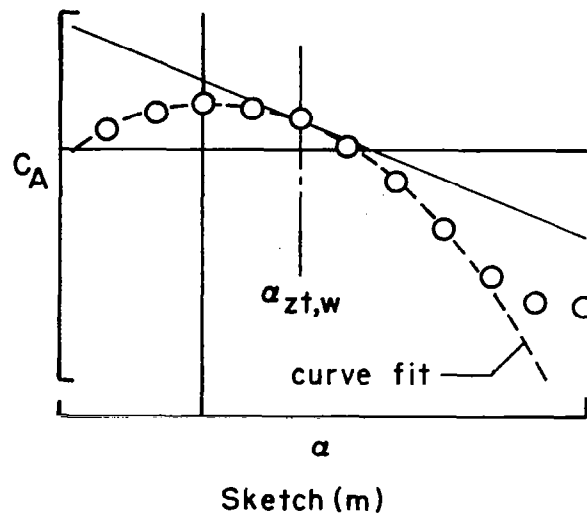
Sketch (1)

$$C_A = k_1 + k_2(\alpha - \alpha_{zt,w}) + k_3(\alpha - \alpha_{zt,w})^2$$

to the experimental axial force data.

An example of Reynolds number extrapolation for the delta wing configurations of reference 7 and figure 12 is given in figure 17. Here the extrapolation is from one wind-tunnel Reynolds number to another. For both the flat and the twisted and cambered versions of this wing-body configuration there is a beneficial Reynolds number effect at least as large as that given by the extrapolation. For the twisted and cambered wing there is evidence of a drastic flow

break-down (perhaps vortex bursting) beyond $\alpha = 8^\circ$ at the lower Reynolds number. The improvement at the higher Reynolds number is much larger than that attributable to leading-edge thrust alone, which suggests an additional Reynolds number benefit related to the overall flow field.



CONCLUDING REMARKS

This report describes numerical methods which have been incorporated into a computer program to provide estimates of the subsonic aerodynamic performance of twisted and cambered wings of arbitrary planform with attainable thrust and vortex lift considerations taken into account. The computational system is based on a linearized theory lifting surface solution which provides a spanwise distribution of theoretical leading-edge thrust in addition to the surface distribution of perturbation velocities. In contrast to the commonly accepted practice of obtaining linearized theory results by simultaneous solution of a large set of equations, the approach used here relies on a solution by iteration. The method also features a superposition of independent solutions for a cambered and twisted wing and a flat wing of the same planform to provide, at little additional expense, results for a large number of angles of attack or lift coefficients.

A previously developed method is employed to assess the portion of the theoretical thrust actually attainable and the portion that is felt as a vortex normal force.

The correlations presented here demonstrate the potential of the present method for application to the subsonic analysis of vehicles designed for supersonic cruise. Vehicles of this class tend to have geometric characteristics that present no significant problems in mathematical modeling. Also for this class of vehicle with relatively thin wing sections, the degree of attainment of leading-edge thrust may vary greatly with changes in geometric properties of the wing and with changes in operational conditions. Thus the present capability for prediction of attainable thrust and vortex effects for twisted and cambered as well as flat wings is a valuable asset. Vehicles designed for subsonic cruise present a more difficult problem. Their thicker wing sections are more difficult to handle properly in the numerical solution without a large number of elements and increased computational costs. Furthermore, the thicker wings tend to produce leading-edge thrust close to the full theoretical values so that estimation of attainable thrust is not as critical a factor. Even so, some of the techniques presented here may prove to be valuable additions to other computational methods that perhaps are more suited to the geometric characteristics of subsonic cruise aircraft.

REFERENCES

1. Carlson, Harry W.; Mack Robert J.; and Barger, Raymond L.: Estimation of Attainable Leading-Edge Thrust for Wings at Subsonic and Supersonic Speeds. NASA TP-1500, 1979.
2. Polhamus, Edward C.: Predictions of Vortex-Lift Characteristics by a Leading-Edge Suction Analogy. J. Aircraft, Vol. 8, No. 4, April 1971, pp. 193-199.
3. Margason, Richard J.; and Lamar, John E.: Vortex-Lattice FORTRAN Program for Estimating Subsonic Aerodynamic Characteritics of Complex Planforms. NASA TN D-6142, 1971.
4. Carlson, Harry W.; and Mack, Robert J.: Estimation of Leading-Edge Thrust for Supersonic Wings of Arbitrary Planform. NASA TP-1270, 1978.
5. Hayes, Wallace D.: Linearized Supersonic Flow. Ph.D. Thesis, California Institute of Technology, 1947.
6. Smith, Willard G.; and Phelps, E. Ray: Lift, Drag, and Pitching Moment of Low-Aspect-Ratio Wings at Subsonic and Supersonic Speeds - Triangular Wing of Aspect Ratio 2 With NACA 0005-63 Thickness Distribution, Cambered and Twisted for a Trapezoidal Span Load Distribution. NACA RM A50K27a, 1951.
7. Phelps, E. Ray; and Smith, Willard G.: Lift, Drag, and Pitching Moment of Low-Aspect-Ratio Wings at Subsonic and Supersonic Speeds - Triangular Wing of Aspect Ratio 4 With NACA 0005-63 Thickness Distribution, Cambered, and Twisted for Trapezoidal Span Load Distribution. NACA RM A50K24b, 1951.
8. Shrout, Barrett L.: Aerodynamic Characteristics of Mach Numbers From 0.6 to 2.16 of a Supersonic Cruise Fighter Configuration With a Design Mach Number of 1.8. NASA TM X-3559, 1977.

9. Decker, John P.; and Jacobs, Peter F.: Stability and Performance Characteristics of a Fixed Arrow Wing Supersonic Transport Configuration (SCAT 15F-9898) at Mach Numbers From 0.60 to 1.20. NASA TM-78726, 1978.
10. Capone, Francis J.: Longitudinal Aerodynamic Characteristics of a Twin-Turbofan Subsonic Transport With Nacelles Mounted Under the Wings. NASA TN D-5971, 1970.
11. Hassell, James L., Jr.; Newsom, William A., Jr.; and Yip, Long P.: Full-Scale Wind-Tunnel Investigation of the Advanced Technology Light Twin-Engine Airplane (ATLIT). NASA TP-1591, 1980.
12. Kjelgaard, Scott O.; and Thomas, James L.: Comparison of Three-Dimensional Panel Methods With Strip Boundary-Layer Simulations to Experiment. NASA TM-80088, 1979.

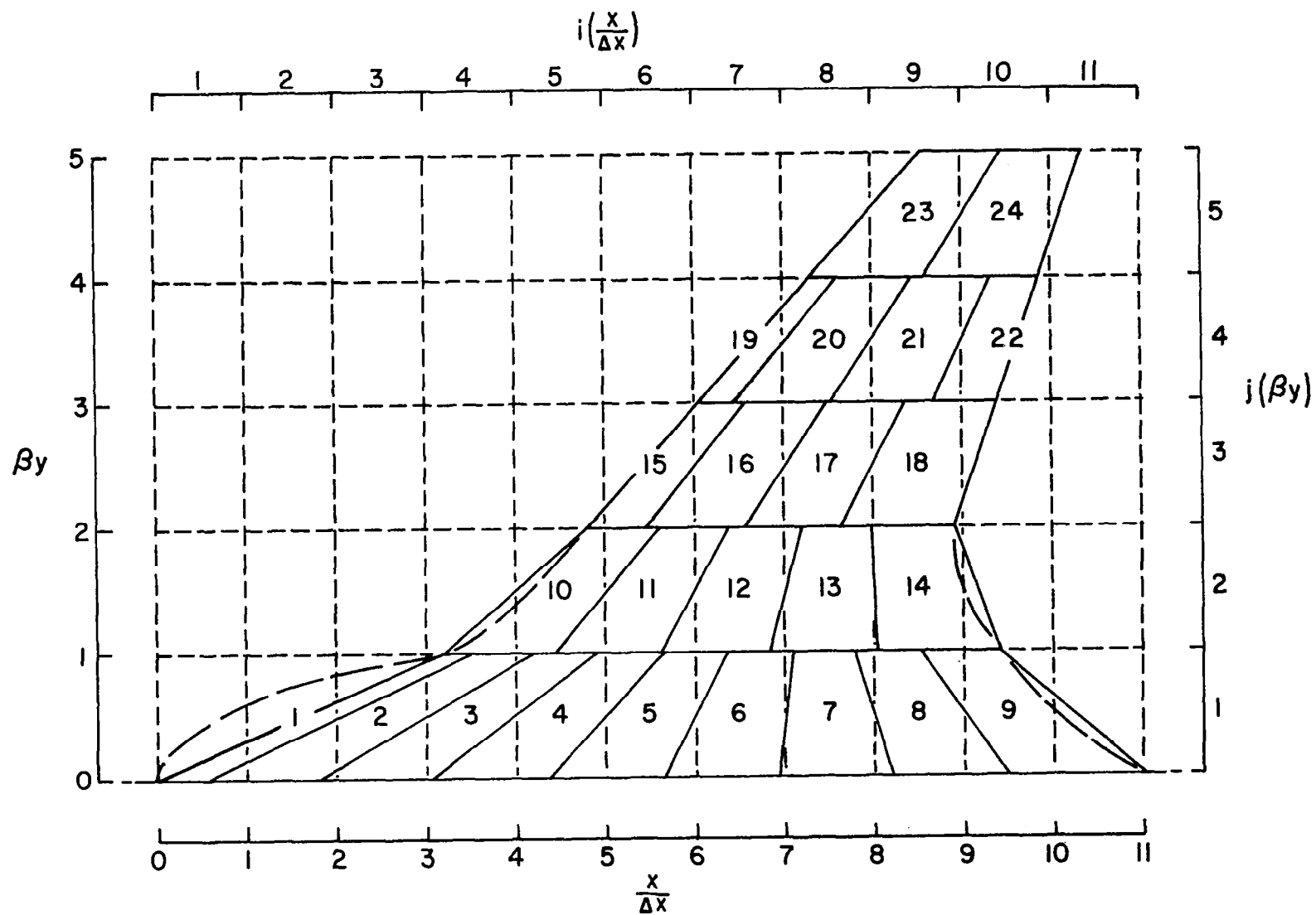


Figure 1. - Grid system used in iterative numerical solution of linearized theory.

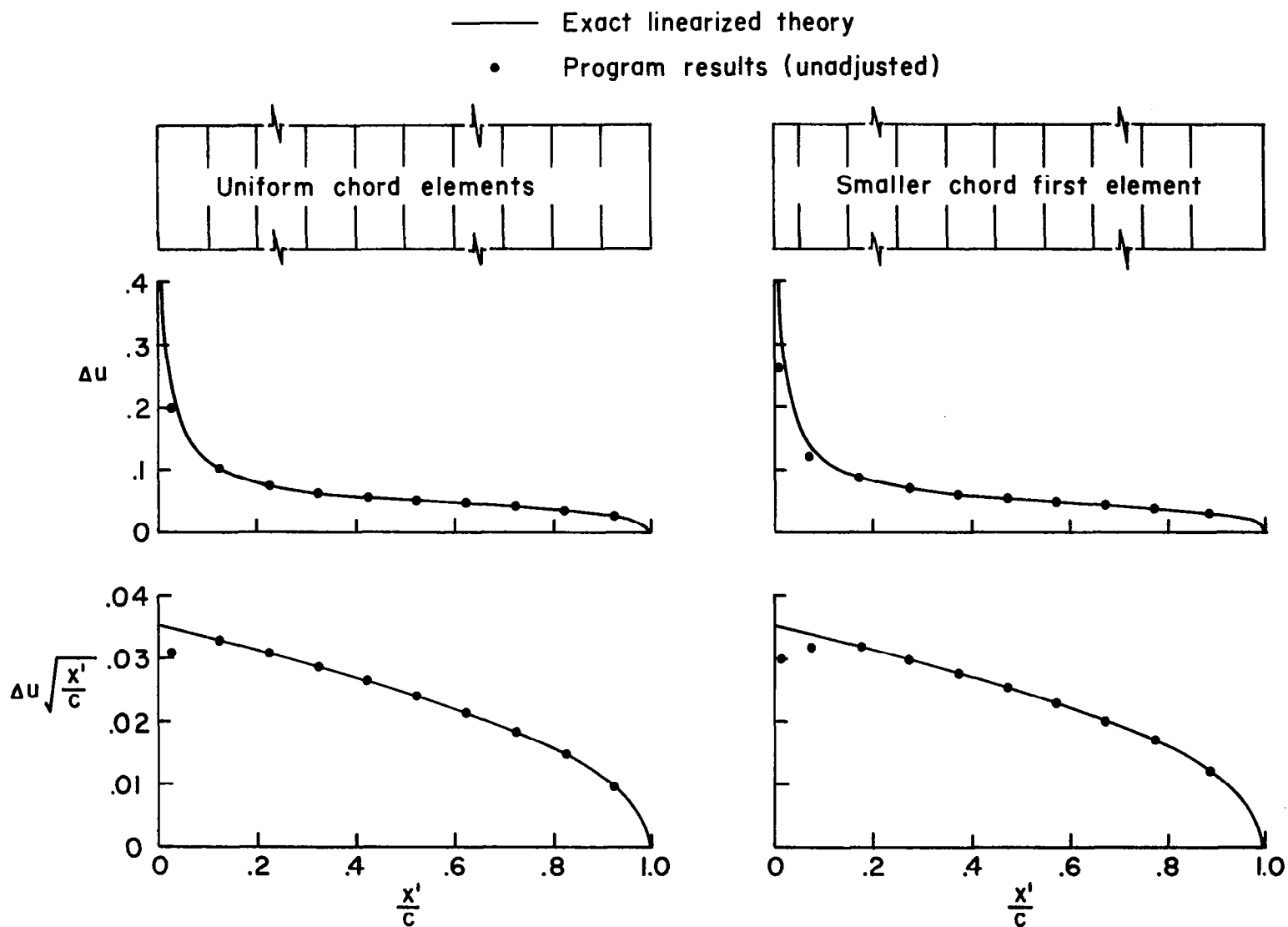
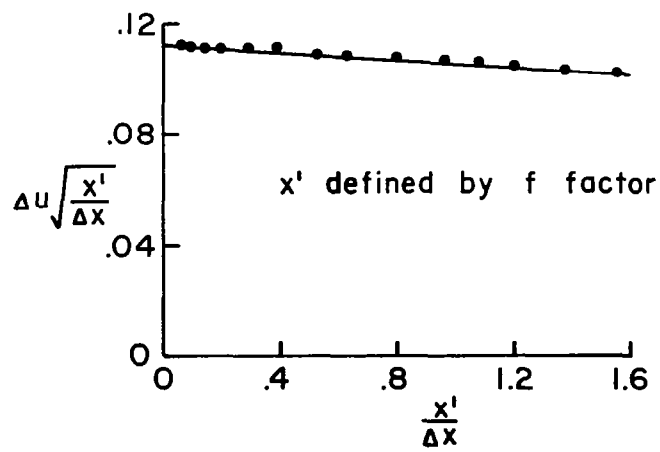
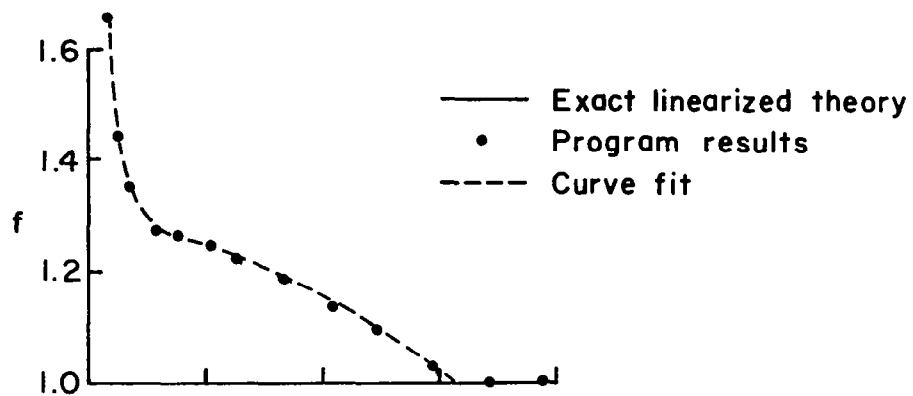
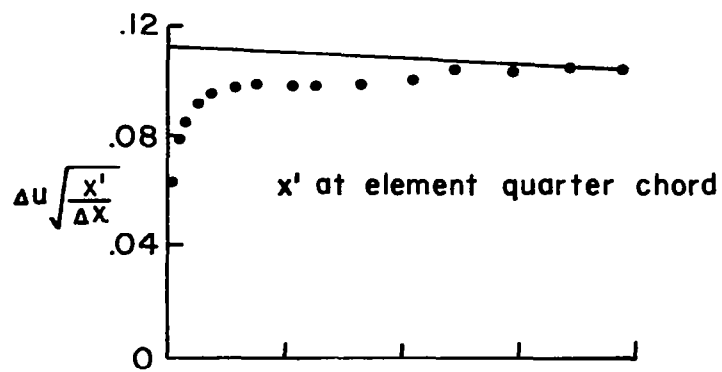


Figure 2. - Typical program results for a flat two-dimensional wing.
 $M = 0$, $\alpha = 1^\circ$.



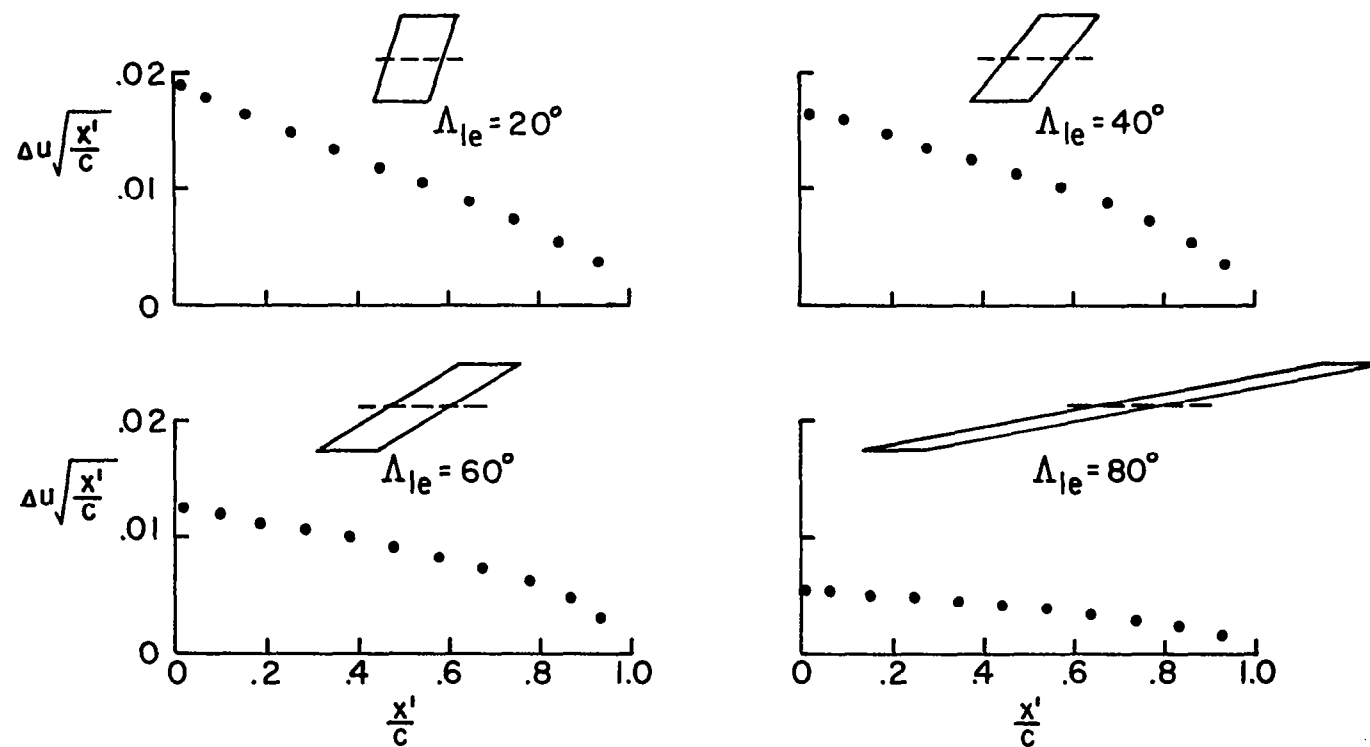
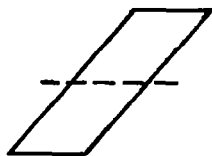


Figure 4. - Program velocity distribution for various sweep angles.
Flat wing. $M = 0$, $\alpha = 1^\circ$



$\Delta_{le} = 40^\circ$

• Program results

----- Fairing of data for 16th iteration

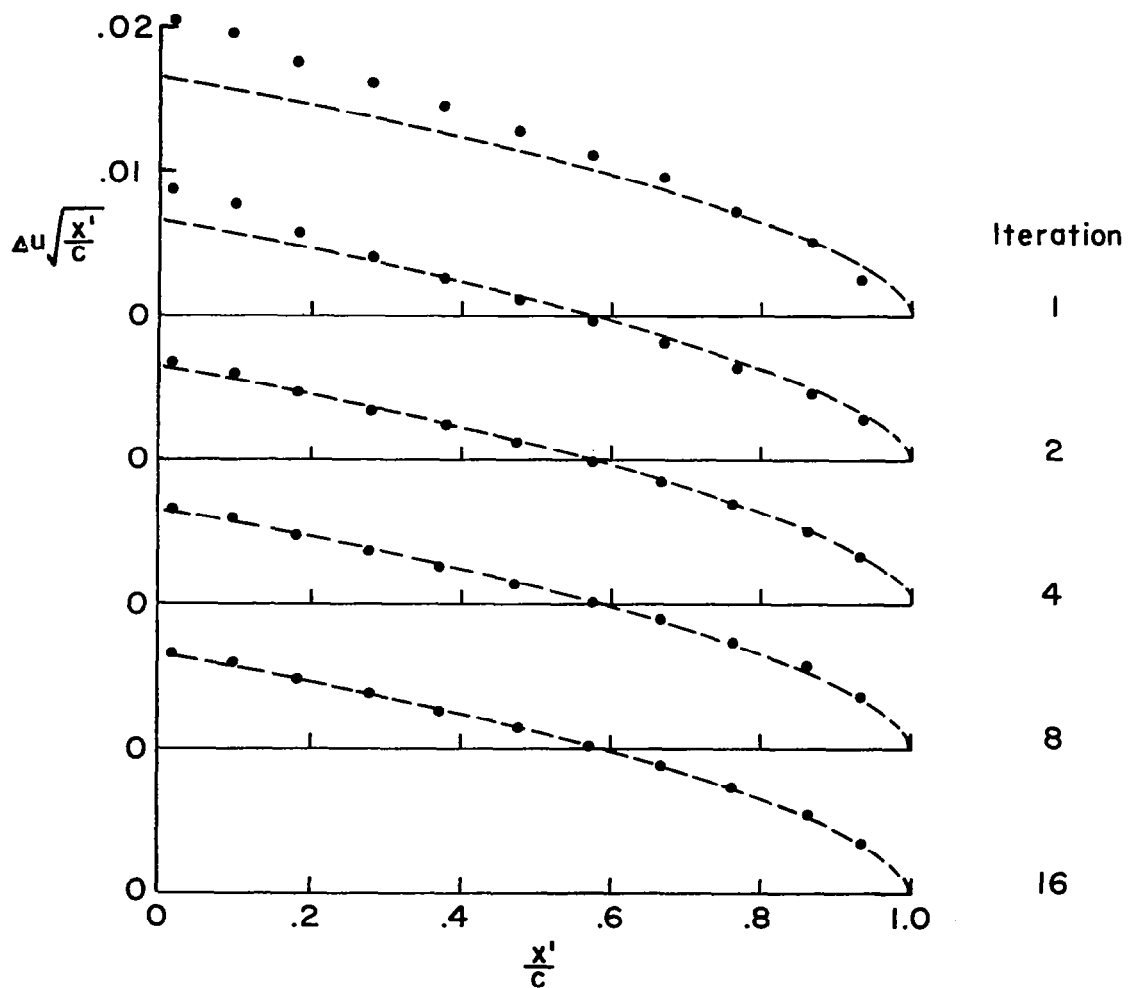


Figure 5. - Illustration of solution convergence.

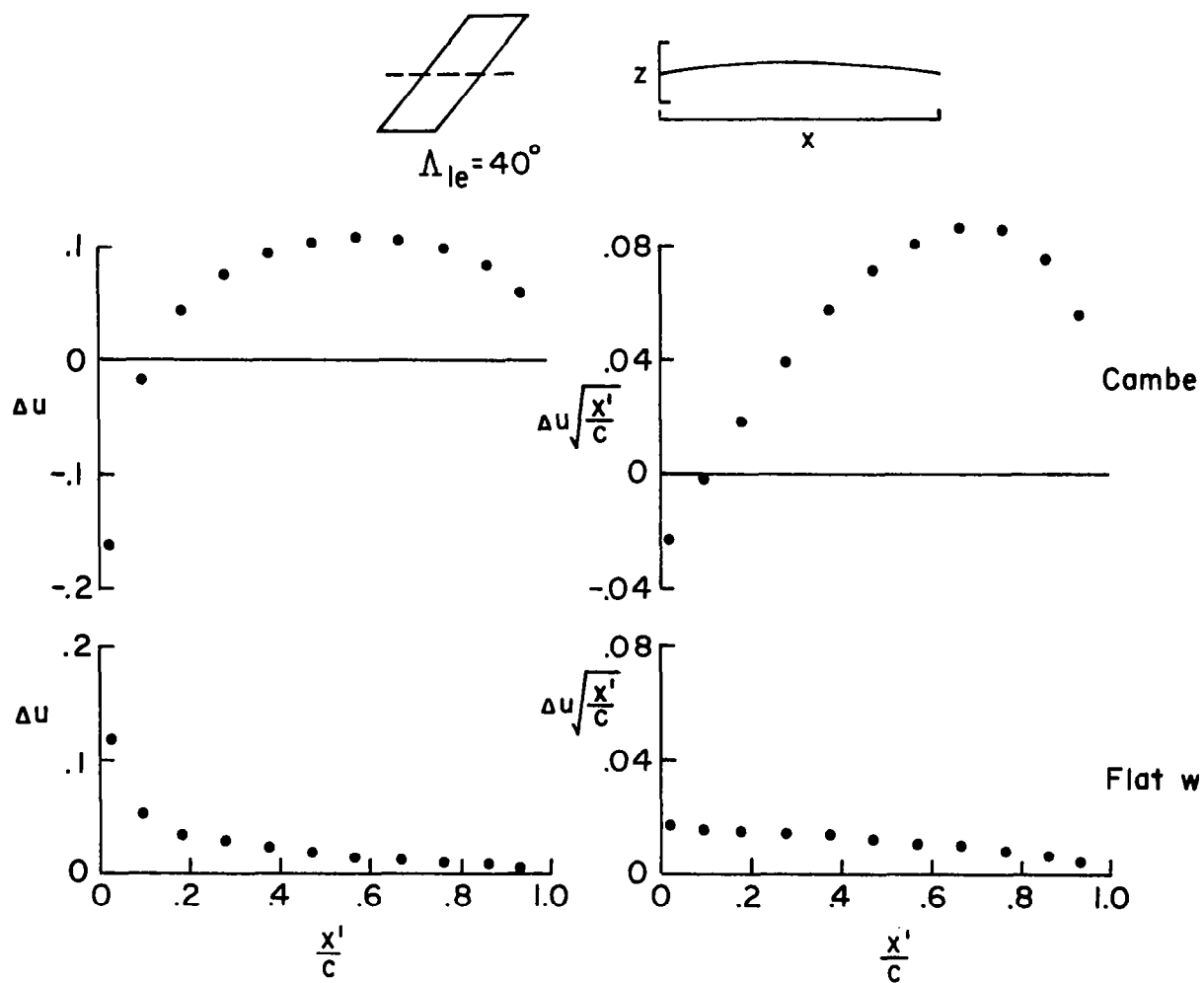


Figure 6. - Program velocity distribution for a cambered wing and a flat wing of the same planform. $M = 0$.

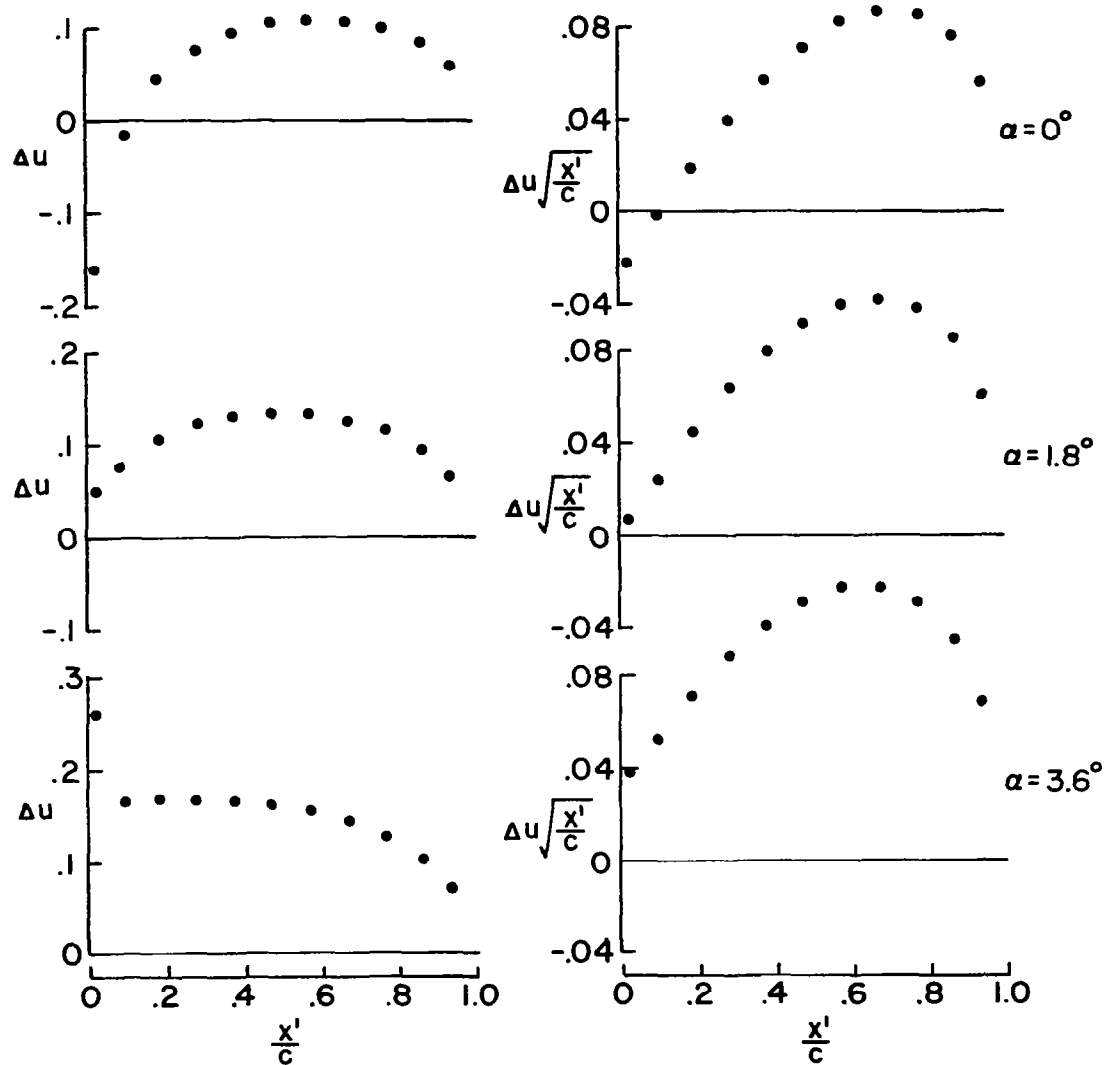


Figure 7. - Program velocity distribution for a cambered wing at several angles of attack by superposition of cambered and flat wing data.

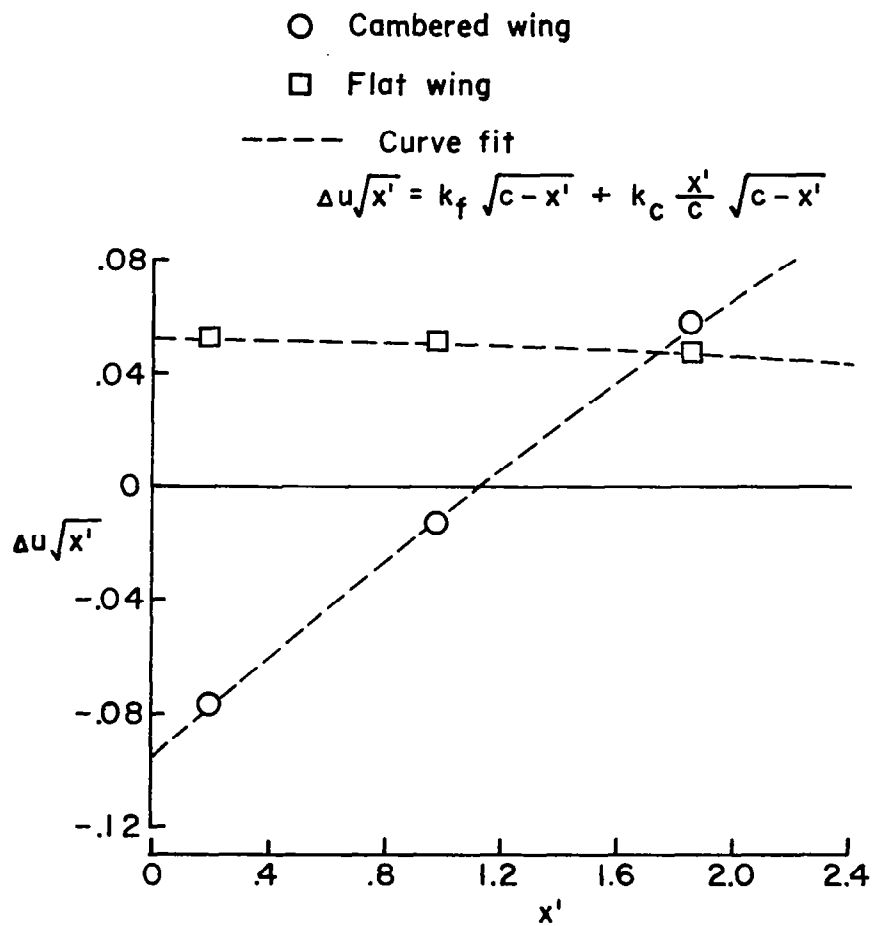


Figure 8. - Illustration of the curve fit used to determine section theoretical thrust coefficients.

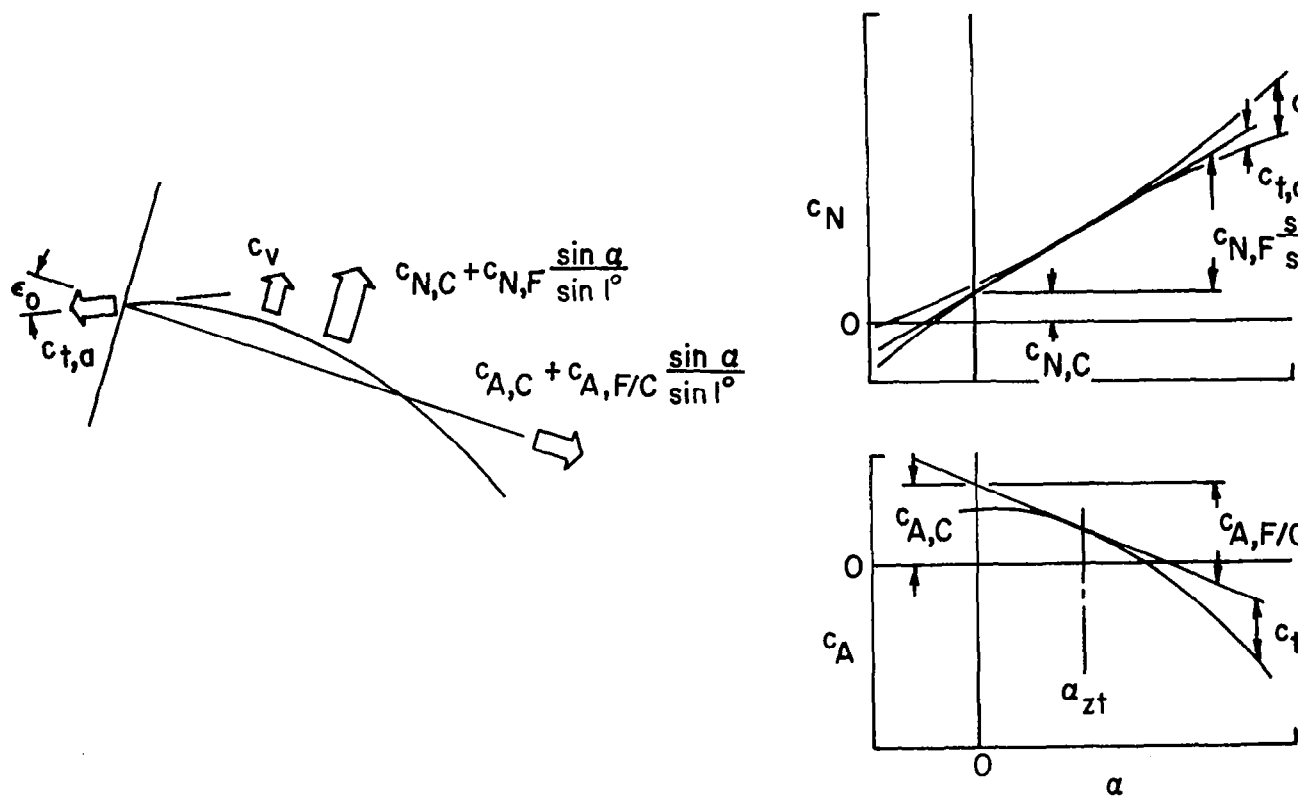


Figure 9. - Build-up of section axial and normal force coefficients.

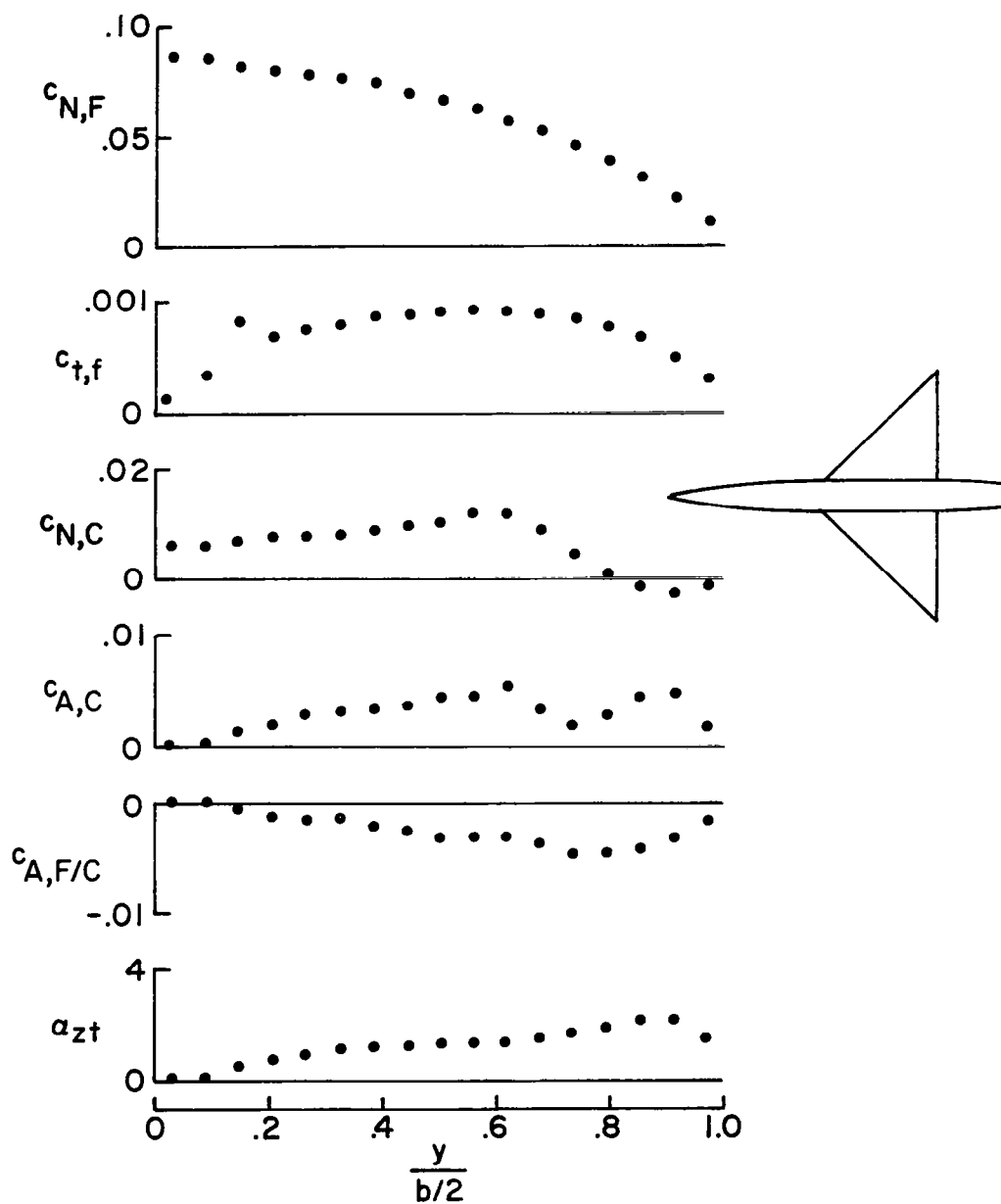
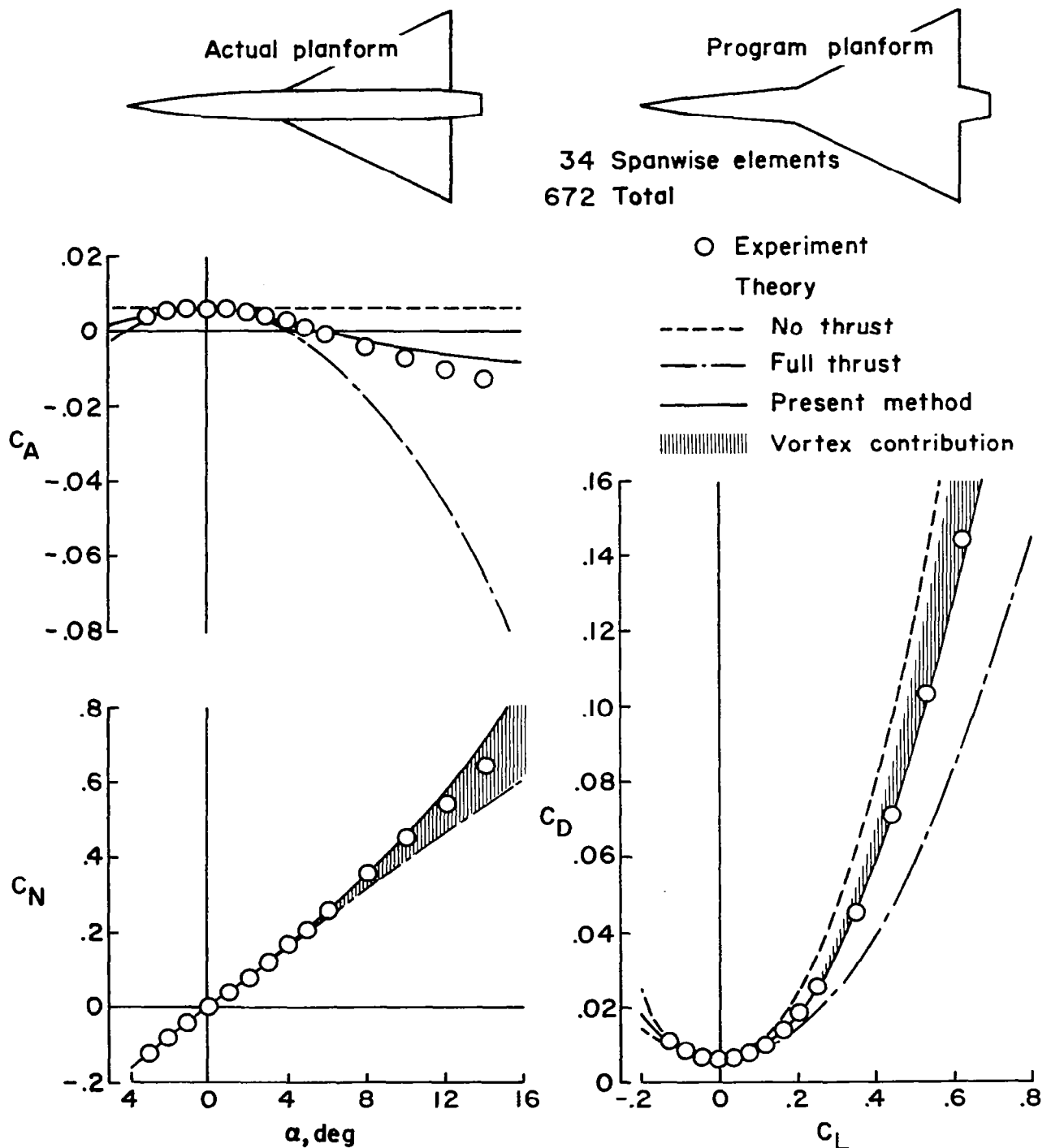
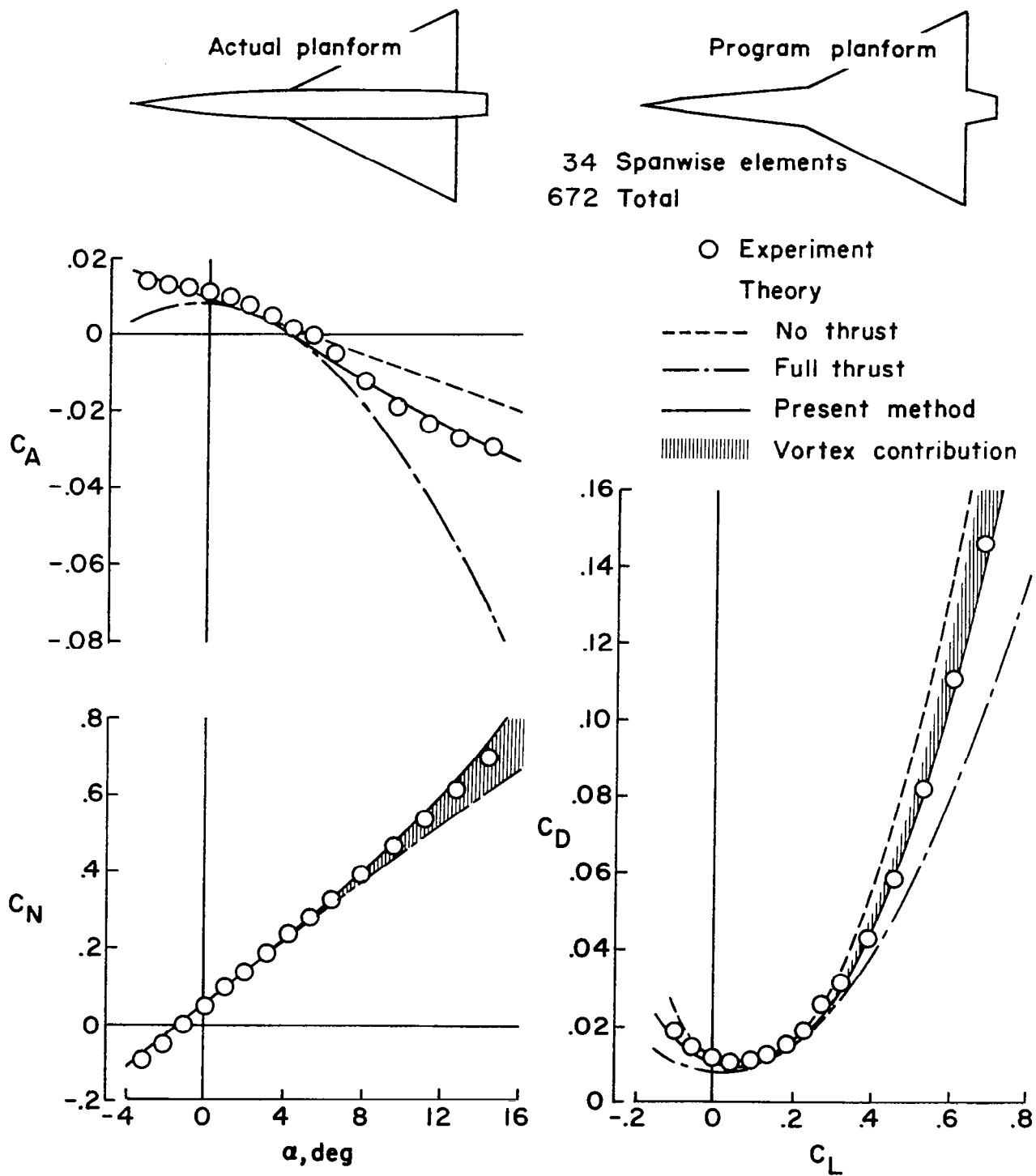


Figure 10. - Spanwise variation of wing section coefficients. AR = 4 wing-body with twist and camber. $M = 0.61$.



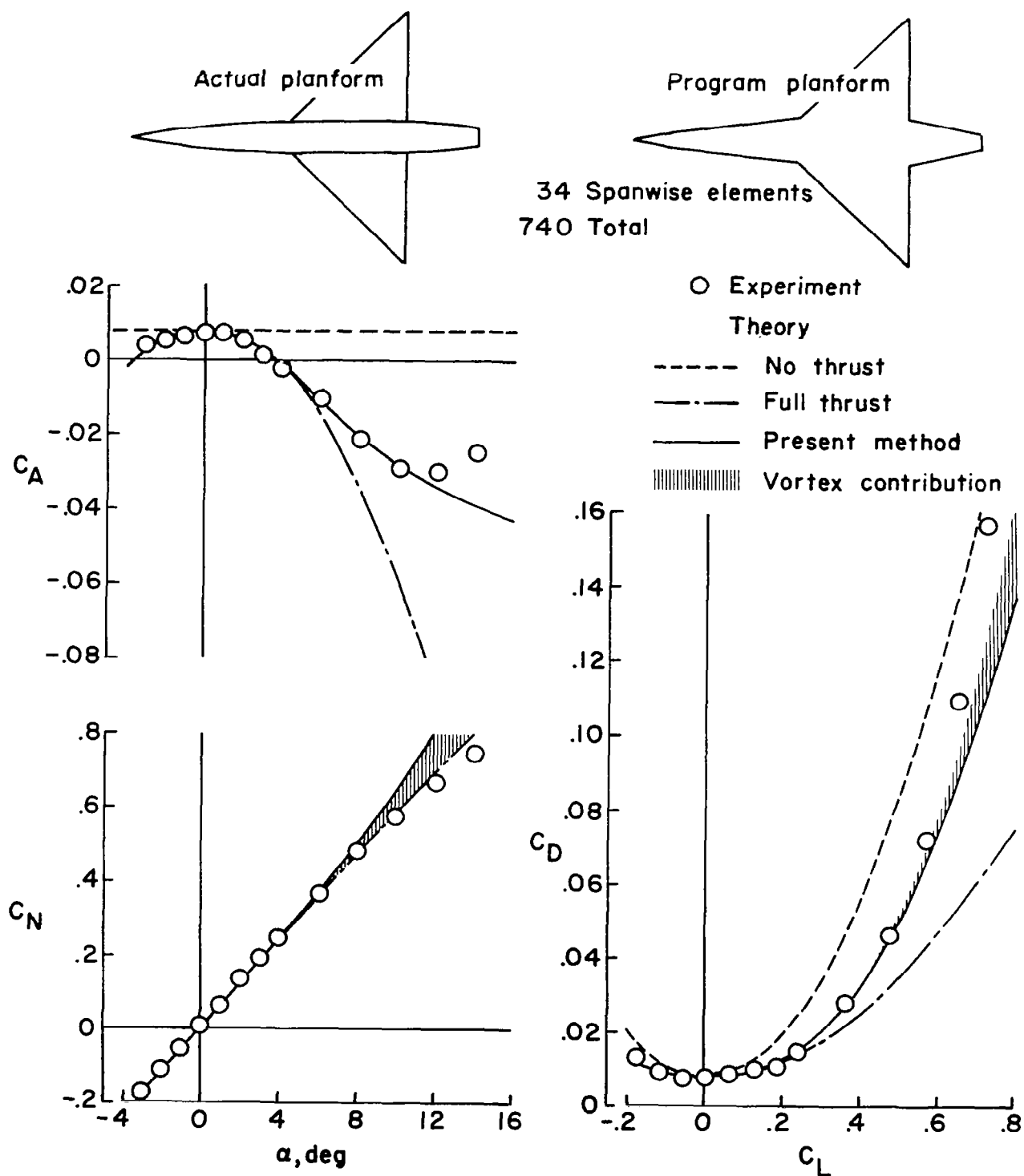
(a) flat wing

Figure 11. - Comparison of theory and experiment for an AR = 2 delta wing-body configuration. $M = 0.61$, $R = 3.0 \times 10^6$.



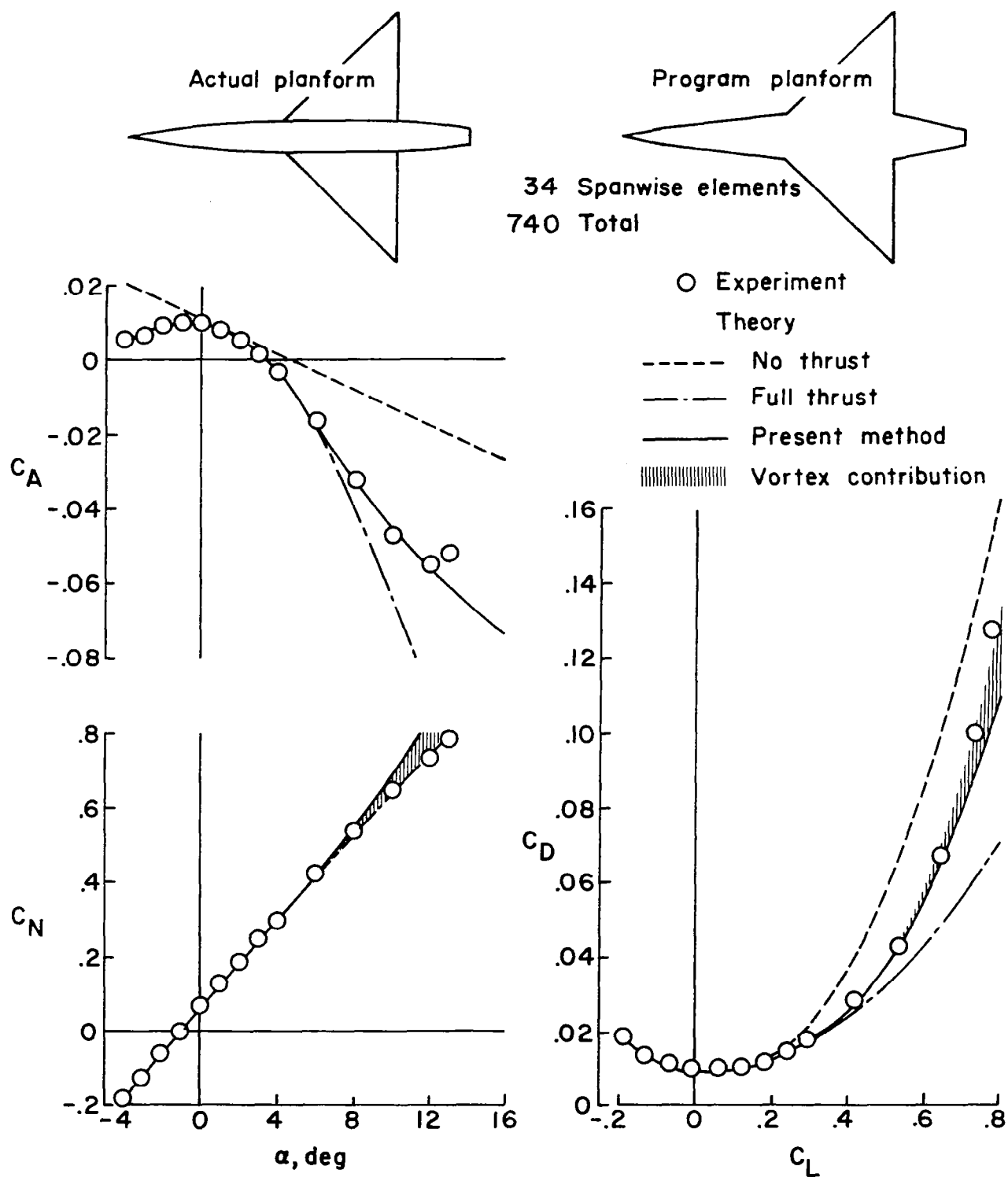
(b) twisted and cambered wing

Figure 11. - Concluded.



(a) flat wing

Figure 12. - Comparison of theory and experiment for an $AR = 4$ delta wing-body configuration. $M = 0.25$, $R = 8.0 \times 10^6$.



(b) twisted and cambered wing

Figure 12. - Concluded.

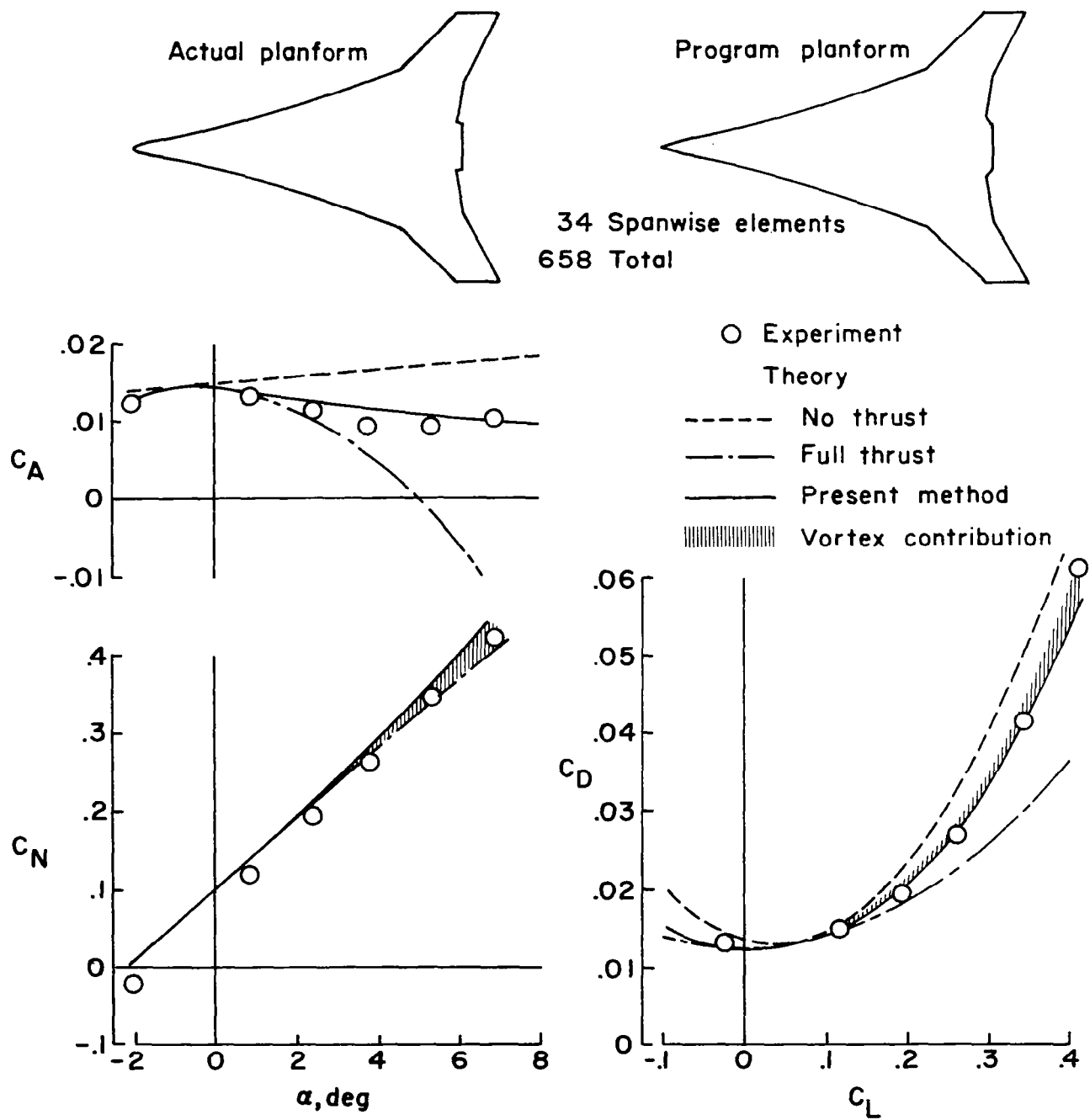


Figure 13. - Comparison of theory and experiment for a supersonic cruise fighter.
 $M = 0.60$, $R = 2.8 \times 10^6$.

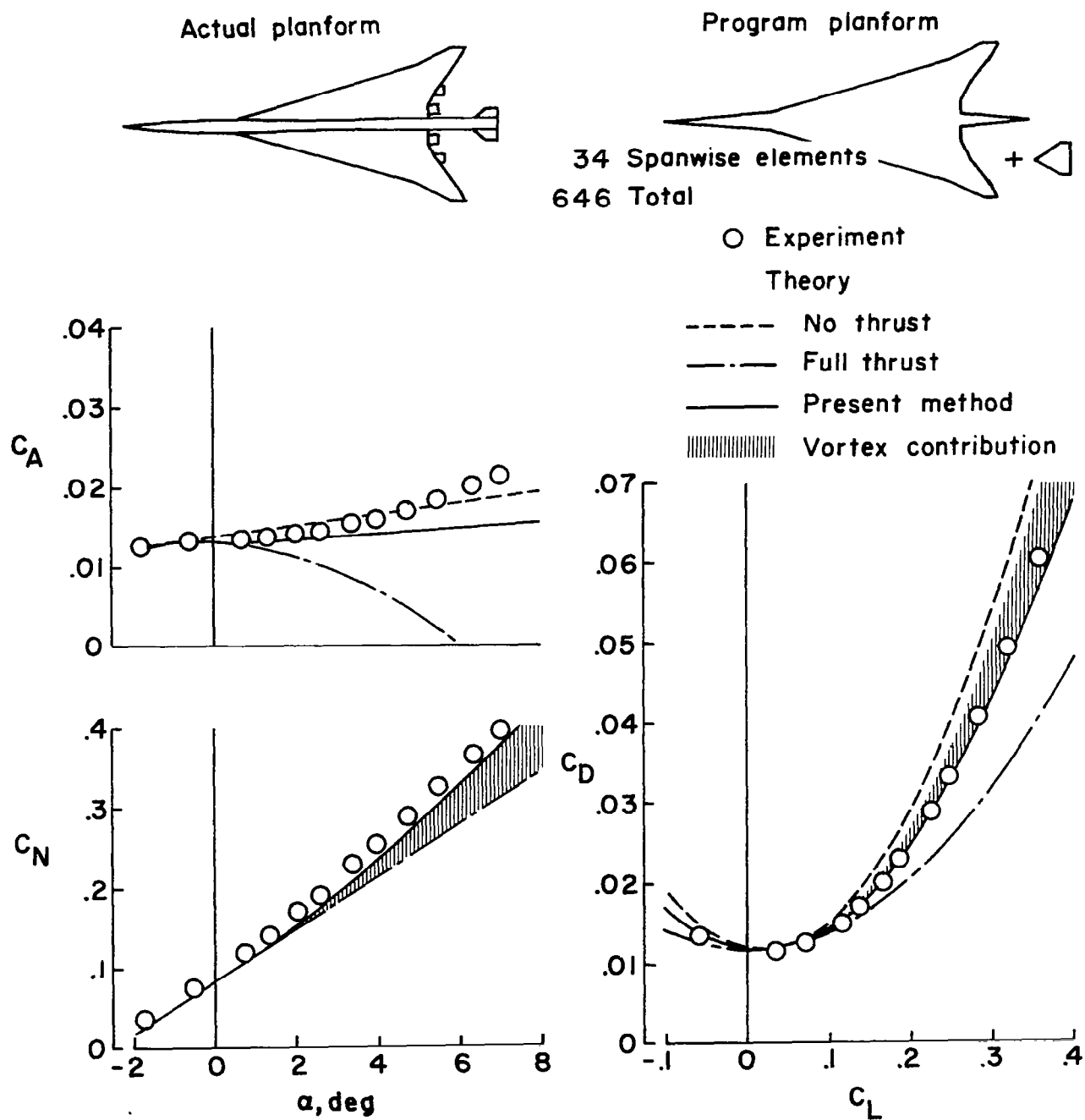


Figure 14. - Comparison of theory and experiment for a supersonic transport.
 $M = 0.60$, $R = 2.0 \times 10^6$.

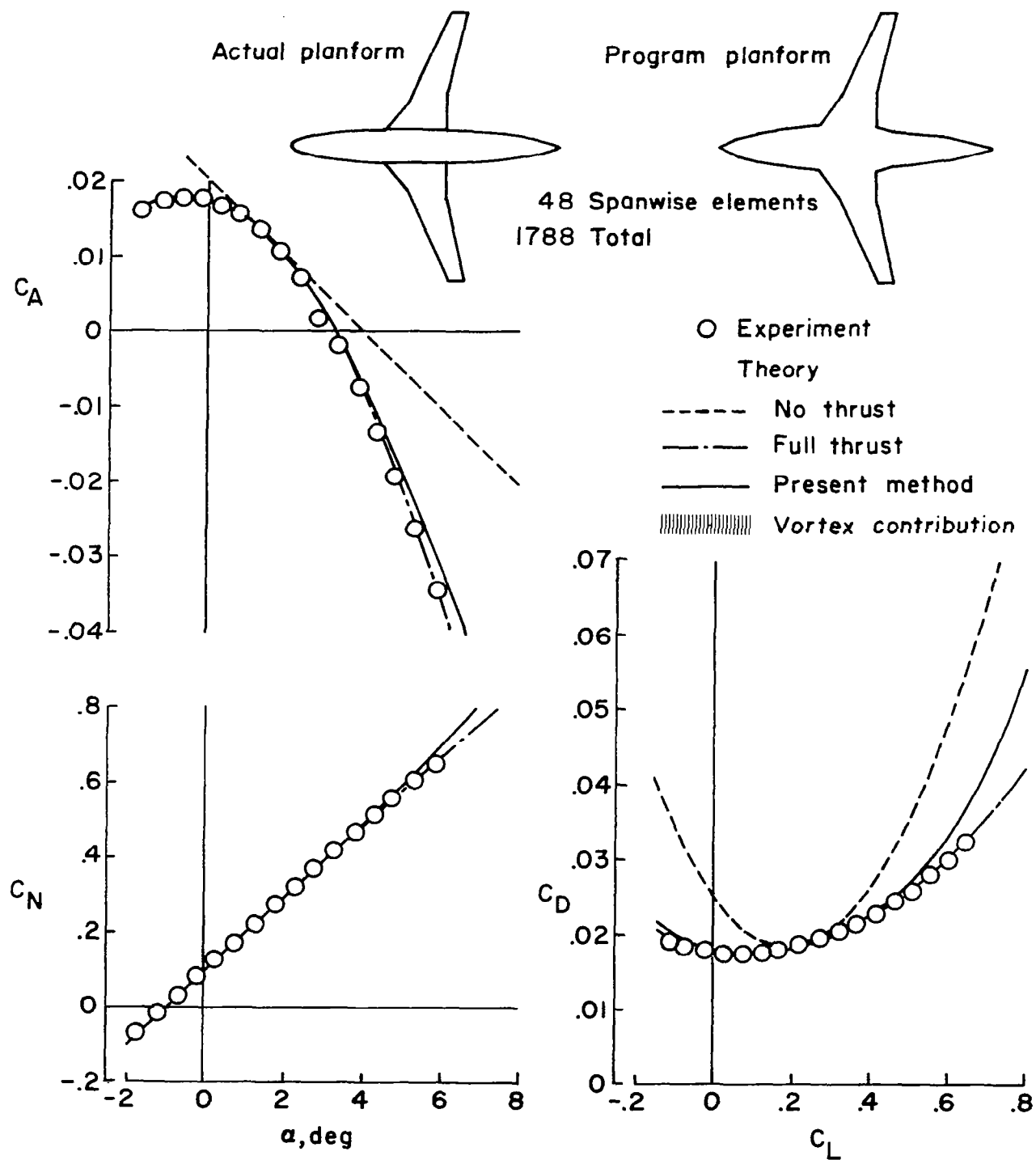


Figure 15. - Comparison of theory and experiment for a subsonic transport wing-body. $M = 0.55$, $R = 2.25 \times 10^6$.

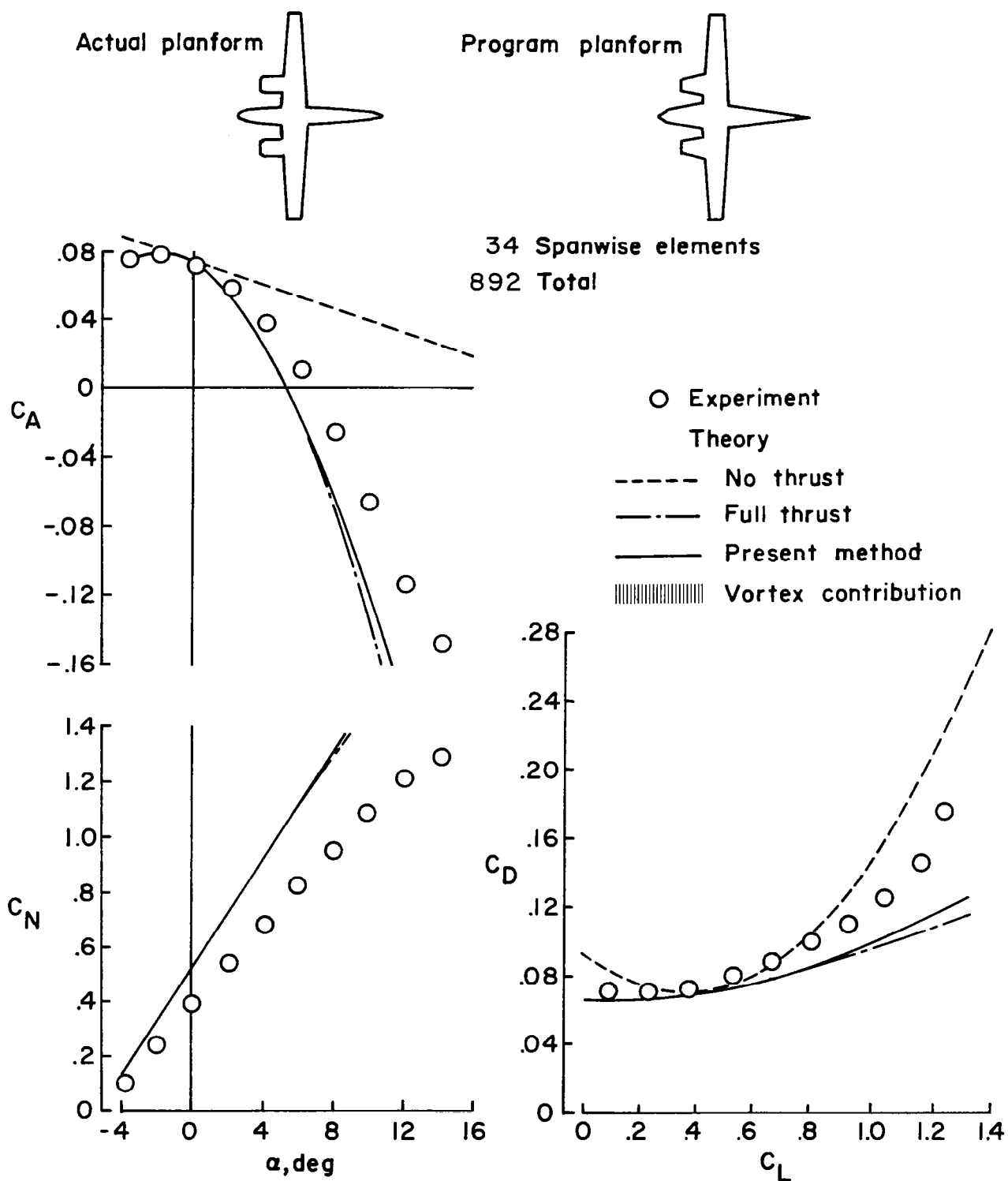


Figure 16. - Comparison of theory and experiment for a twin engine private airplane. $M = 0.12$, $R = 2.3 \times 10^6$.

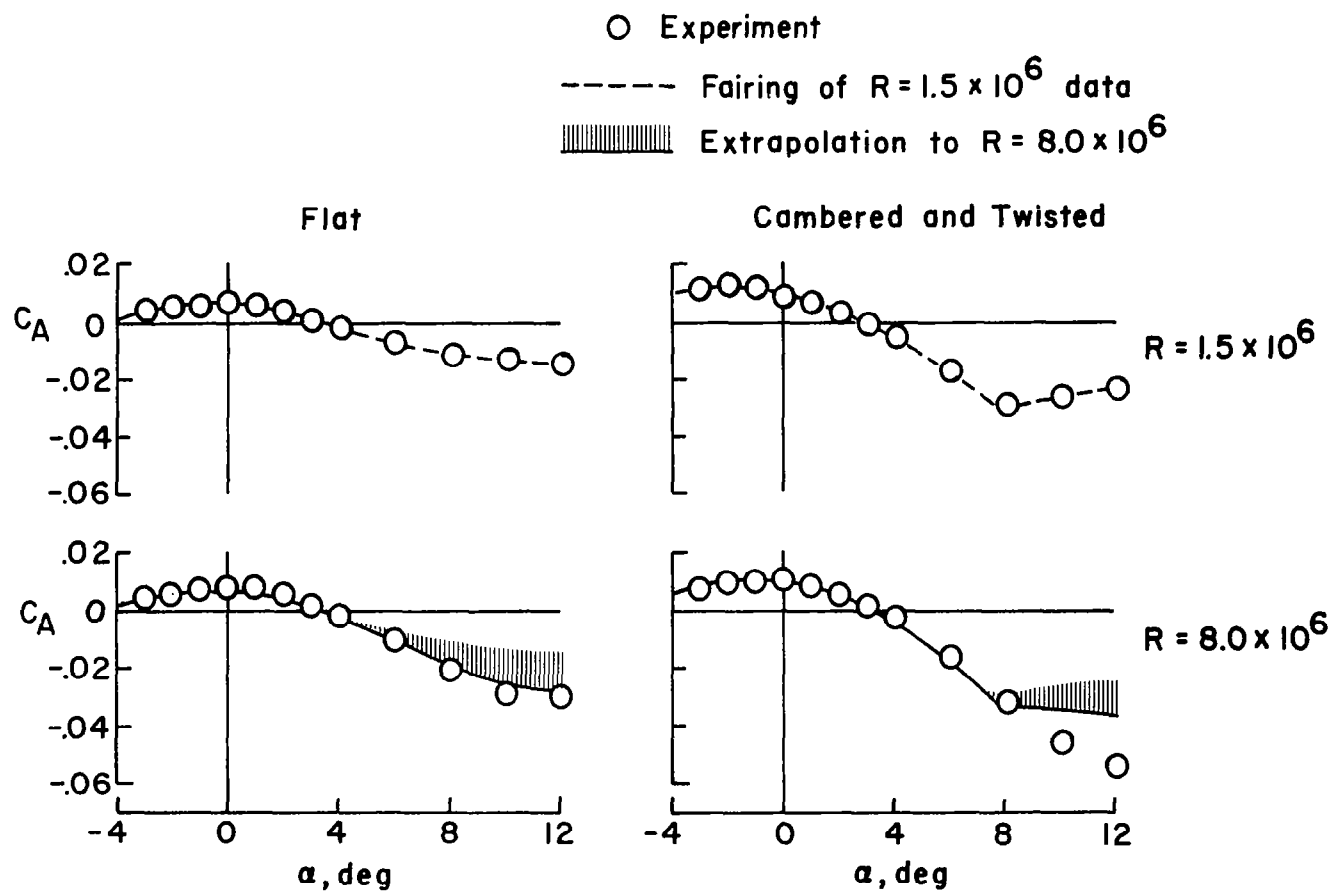


Figure 17. - An example of Reynolds number extrapolation. $AR = 4$ Delta wing-body.
 $M = 0.25$.

1. Report No. NASA CR-3515		2. Government Accession No.		3. Recipient's Catalog No.	
4. Title and Subtitle A COMPUTER PROGRAM FOR WING SUBSONIC AERODYNAMIC PERFORMANCE ESTIMATES INCLUDING ATTAINABLE THRUST AND VORTEX LIFT EFFECTS				5. Report Date March 1982	
				6. Performing Organization Code	
7. Author(s) Harry W. Carlson and Kenneth B. Walkley				8. Performing Organization Report No.	
				10. Work Unit No.	
9. Performing Organization Name and Address Kentron International Incorporated Hampton Technical Center Hampton, VA 23666				11. Contract or Grant No. NAS1-16000	
				13. Type of Report and Period Covered Contractor Report	
12. Sponsoring Agency Name and Address National Aeronautics and Space Administration Washington, DC 20546				14. Sponsoring Agency Code 533-01-43-01	
15. Supplementary Notes Langley Technical Monitor: Samuel M. Dollyhigh Interim Report					
16. Abstract This report describes numerical methods which have been incorporated into a computer program to provide estimates of the subsonic aerodynamic performance of twisted and cambered wings of arbitrary planform with attainable thrust and vortex lift considerations taken into account. The computational system is based on a linearized theory lifting surface solution which provides a spanwise distribution of theoretical leading-edge thrust in addition to the surface distribution of perturbation velocities. In contrast to the commonly accepted practice of obtaining linearized theory results by simultaneous solution of a large set of equations, the approach used here relies on a solution by iteration. The method also features a superposition of independent solutions for a cambered and twisted wing and a flat wing of the same planform to provide, at little additional expense, results for a large number of angles of attack or lift coefficients. A previously developed method is employed to assess the portion of the theoretical thrust actually attainable and the portion that is felt as a vortex normal force.					
17. Key Words (Suggested by Author(s)) Subsonic aerodynamic Numerical methods Leading-edge thrust			18. Distribution Statement Unclassified - Unlimited Subject Category 01		
19. Security Classif. (of this report) UNCLASSIFIED	20. Security Classif. (of this page) UNCLASSIFIED	21. No. of Pages 60	22. Price A04		